A Two-Scale Thermomechanical Computational Model for Reinforced Concrete Frame Structures

A THESIS
SUBMITTED TO THE FACULTY OF THE GRADUATE SCHOOL
OF THE UNIVERSITY OF MINNESOTA
BY

Marie DesHarnais

IN PARTIAL FULFILLMENT OF THE REQUIREMENTS
FOR THE DEGREE OF
MASTER OF SCIENCE

Jia-Liang Le

September, 2014

Acknowledgements

My thanks go to my advisor, Dr. Jia-Liang Le, for all his guidance in this project, and to my fellow graduate student, Bing Xue, who helped considerably in the simulation work in ABAQUS. I am also grateful to Dr. Sze Dai Pang, his students, Dr. Hongjian Du, and the structures lab staff at the National University of Singapore for hosting me and provided the opportunity for me to perform material testing for this project.

The computer modeling I describe would not have been possible in the time available to me if it were not for the University of Minnesota Supercomputing Institute. I would also like to thank the US National Science Foundation (NSF) and National Research Foundation (NRF) of Singapore and their EAPSI program which provided the funding for the material testing in Singapore.

Abstract

A two-scale numerical model is developed to study the behavior of reinforced concrete (RC) frame structures subject to fire loading. In this model, various structural components, such as beams, columns, and beam-column joints, are modeled by elastic elements connected by a set of nonlinear cohesive elements, which represent the potential damage zones. The thermo-dependent constitutive behavior of each cohesive element is determined by nonlinear finite elements (FE) simulations of its corresponding potential damage zone under different loading modes at different temperatures, where the thermo-dependent material properties for the FE simulations are determined based on the existing literature and a set of high-temperature experiments on concrete. The proposed two-scale model is used to simulate the behavior of a RC frame subassemblage under thermomechanical loading and the simulation results are further compared with the prediction by using the conventional finite element model. It is shown that the present model can well capture the nonlinear behavior of RC frame structures under thermomechanical loading, and due to its computational efficiency, the model provides us an efficient means to investigate the global behavior of large-scale RC frame structures under fires.

Contents

List of Tables

List of Figures

Chapter 1

Introduction

According to the National Fire Protection Agency, about 1,375,000 fires occurred in the United States in 2012 costing 2,855 civilian lives and 12.4 billion US dollars in direct property losses [1]. The United States' National Institute of Technology and Standards (NIST) conducted a study in 2002 to analyze the need to study full-scale fire resistance, and the capacity to perform this research within the United States [2]. As part of the study, a survey of building failures caused by fire was compiled, including a number of collapses of reinforced concrete (RC) structures. Two of the cases recorded by NIST are shown in Fig. 1.1, and further examples are given in Table 1.1. The NIST study concluded that there is a pressing need in the US for a better understanding of structural integrity of buildings under fire conditions.

An extensive fire in a building can cause local structural damage which can potentially lead to cascading failures of the building structure. This is usually referred to as the progressive collapse. Different from conventional design where structural elements can be designed to withstand certain loads, analysis and design of buildings against progressive collapse require fundamental understanding of the global behavior of the entire building subjected to some local structural damage.

In the past decade, extensive efforts have been devoted to developing computational models containing different levels of details. The full-scale continuum finite element (FE) simulation of progressive collapse can capture the detailed nonlinear structural behavior directly from the material constitutive relationships, but the computational cost is usually very high, especially for large-scale buildings [3]. In a recent study [4], a

Building Name	**Location; Date**	**Description of Building and Collapse**
Apartment block	St. Petersburg, Russia; June 3, 2002	Concrete, total collapse starting 1 hour fire duration
Jackson Street Apartments	Hamilton, Ontario, Canada; Feb. 8, 2002	Concrete, partial collapse of concrete floor-ceilings
Pentagon	Washington, DC, USA; Sept. 11, 2001	RC, partial collapses of floors and members, 30 minutes after jet impact
Textile Factory	Alexandria, Egypt; July 21, 2000	RC, no sprinklers, total collapse 9 hours after fire
CESP, Sede 2	Sao Paulo, Brazil; May 21, 1987	RC frame, with ribbed slabs, no sprinklers. Partial collapse, full height interior core collapse, after 2 hour fire
Katrantzo Sport Department Store	Athens, Greece; Dec. 19, 1980	RC, partial collapse of 5th-8th floor, together with other members, during a 2-3 hour fire
Military Personnel Record Center	Overland, MO, USA; July 12, 1973	RC, without expansion joints, no sprinklers above 2nd floor. Roof and supporting columns partially collapsed 12 hours after fire began

Table 1.1: NIST survey of RC structure failures due to fire[2].

discrete element model was developed to simulate the nonlinear structural behavior as well as debris impact, where the beams, columns and slabs were represented by spheres connected by springs. Similar to the FE simulations, the main limitation of the discrete element model is the high computational cost. By contrast, simplified numerical models have been proposed to achieve a balance between model accuracy and computational affordability. Early approaches include the formulation of a damage-dependent beam element within the framework of the slope-deflection method [5, 6]. Recent efforts have focused on the development of a macro-element model [7, 8], where the beam-column connections are modeled by a set of uncoupled springs. The constitutive behavior of these springs is calibrated from the material constitutive behavior in the direction of the individual spring. This model was first developed for 2-D steel and RC frames [7, 8], and was later extended to 3-D steel buildings [3]. However, these existing numerical

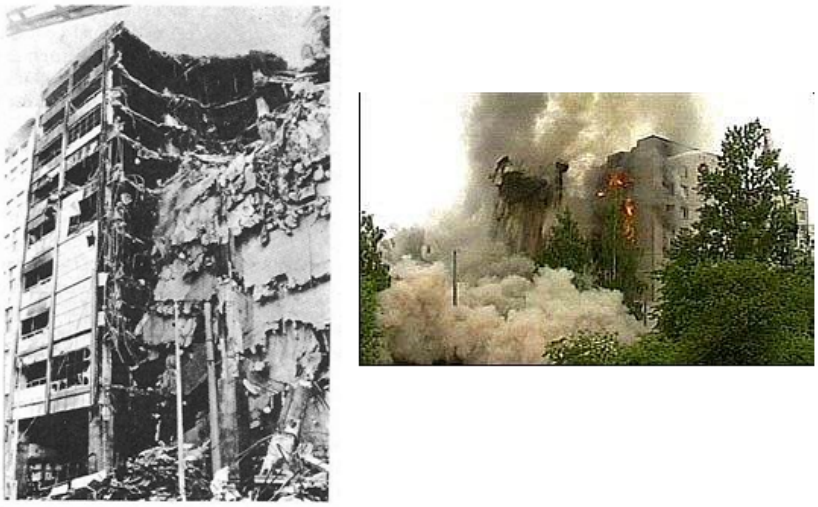

Figure 1.1: Katrantzos Department Building in Athens, Greece (1980, left), and collapse of a burning apartment block in St. Petersburg, Russia (2002, right)[2].

models were all developed and used for analysis of progressive collapse of buildings that are subjected to local structural damage due to mechanical loading.

During the past three decades, numerous experiments have demonstrated that various mechanical and thermal properties of concrete, such as elastic modulus, compressive strength, fracture energy, and thermal conductivity [9, 10], are strongly dependent on the temperature [11, 12, 13]. This temperature dependence is in part due to changes in the structure of the cement paste such as loss of water and decomposition of the calcium hydroxide, but also is a result of stress relaxation from thermal expansion and potential stress induced by thermal gradients [13, 14].In parallel with many experimental investigations, substantial efforts have also been directed to developing constitutive models for concrete at elevated temperatures, which incorporate the aforementioned temperature dependence into a continuum framework [11, 15, 16], and these model can be easily used for finite element simulations of the thermomechanical behavior of concrete materials. Meanwhile, there have also been some limited attempts to mesoscale modeling of concrete at elevated temperatures, which gives more insights into the thermomechanical damage mechanisms [17, 18].

Case studies have investigated the effect of fire on concrete observed in well document events, including the Chunnel fire [19, 14], and the Windsor Tower fire [20]. The existing

numerical tools were largely used for individual structural elements [21, 22, 23] and for small reinforced concrete structures such as chimneys [24] and containment vessels [25, 26]. It is evident that direct applications of finite element or discrete element models for large-scale RC buildings subjected to fires could be severely hindered by the excessive computational cost. Therefore, it is imperative to develop an efficient thermomechanical computational model that can be used for simulation of the global behavior of RC buildings against fires, which includes both local structural damage as well as large-scale structural collapse.

The objective of this research is to develop a two-scale thermomechanical model for RC frame structures, based on a recently proposed numerical model for progressive collapse of RC frame structures. The main feature of the present model is that it can efficiently capture the nonlinear behavior of the RC frame structures at high temperatures, and therefore provides us a means to simulate the global behavior of RC buildings under fires. This thesis is planned as follows: Chapter 2 presents the formulation of the proposed two-scale computational model; Chapters 3 presents a set of high-temperature tests on concrete properties, which are inputted into the present computational model; In Chapter 4, the detailed calibration process for the proposed two-scale model is described; Chapter 5 validates the present model by simulating the nonlinear behavior of RC frame subassemblage subjected to combined thermomechanical loading and comparing it with the conventional finite element simulation; and Chapter 6 summarizes the conclusions drawn from this research.

Chapter 2

Thermo-Dependent Cohesive Modeling of RC Frames

Le and Xue have recently developed an efficient computational model for probabilistic analysis of RC frame structures against progressive collapse [27]. In this model, the structural frame is modeled by elastic elements connected with a set of nonlinear cohesive elements, which represents the potential damage zones that could form during the loading process. In this study, this model is extended to modeling of RC frame structures under general thermomechanical loading. The thermo-dependent constitutive relationship is fully calibrated by fine-scale numerical simulations of the potential damage zones at different temperatures.

2.1 Formulation of Cohesive Model for RC Frames

The concept of cohesive modeling was pioneered by Barenblatt [28] and Dugdale [29], and since then it has been widely used by the fracture mechanics community for investigating nonlinear fracture process in concrete, i.e. [30, 31]. The essential idea behind the cohesive models is that it smears a finite-size damage zone at the crack tip into a zero-thickness nonlinear element whereas the rest part of the structure is considered to behave linear elastically. This provides an efficient means to simulate the nonlinear fracture and damage processes in concrete materials. In this research, we propose to

extend this concept to modeling of RC frame structures under general thermomechanical loading. In the development of such a model, it is necessary to identify the potential damage zones that could form in various structural components, such as beams, columns and beam-column joints, during the loading process. These potential damage zones are modeled by cohesive elements whereas the rest part of the structure is modeled by elastic elements. In other words, the nonlinear behavior of the global structural components is fully captured by these cohesive elements.

In this study, the locations of the potential damage zones are determined based on the existing knowledge of the failure behavior of beams, columns and beam-column joints. For beams, both single and double curvature failure are made possible by placing potential damage zones at ends, midspan, and quarter-spans. In the columns, damages zones are placed following the Shanley column model[32, 33], at both ends and mid-height. The depth of the damage zones are $0.85D_e$ and $0.75D_e$ for beams and columns, respectively. Here D_e is the effective depth of the element, which is equal to the distance between the centroid of the tensile reinforcement and the extreme material fiber in compression [34]. In the joints between beams and columns, the damage zones are located to capture the experimentally observed diagonal cracking [35]. Fig. 2.1 shows the representation of a RC frame subassemblage using the proposed cohesive model.

It should be noted that, different from the conventional cohesive model for concrete materials, where the cohesive properties are directly related to the material fracture properties, the constitutive relationship of the cohesive element determined from the behavior of the individual potential damage zone, which is determined by both material properties and structural geometry. Therefore, the present model is able to capture the effect of structure size on the failure behavior of the structural components, which is essential for modeling of fracture and damage of RC structures [31].

In the proposed model, each cohesive element consists of two Gauss points with potentially distinct constitutive behaviors to reflect the asymmetric distribution of reinforcement, which is commonly found in RC beams. These two Gauss points allow the cohesive element to simulate load-displacement behavior of the potential damage zone in bending, as well as tension, compression, shear, and combinations of these load types. The Gauss points of the cohesive model are calibrated to match the potential damage zone behavior by simulating the corresponding damage zone with a fine-scale

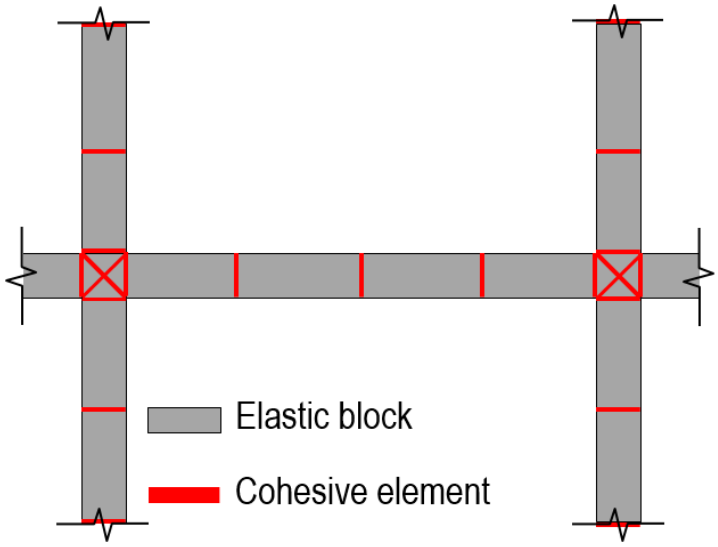

Figure 2.1: Cohesive element locations in Subassembly Model.

model. To perform this calibration, the potential damage zone is broken down into two parts, illustrated in Fig. 2.2. The first part is an effective concrete section, made up of the concrete and the transverse reinforcement, and the second part simply represents the longitudinal reinforcement (Fig. 2.4). The constitutive equations can be written as in Eq. 2.1 and 2.2.

$$\sigma_n = \sigma_n^c(w_{n1}, w_s) + \rho_s \sigma_n^s(w_{n2}, w_s) \tag{2.1}$$

$$\tau = \tau^c(w_{n1}, w_s) + \rho_s \tau^s(w_{n2}, w_s) \tag{2.2}$$

where σ_n, τ are the normal and shear tractions of the Gauss point, σ_n^c, τ^c are the normal and shear cohesive tractions of the effective concrete section, σ_n^s, τ^s are the normal and shear cohesive tractions of the longitudinal reinforcement, $w_{n1} = w_n - \alpha_c(T_s - T_0)L_p$, $w_{n2} = w_n - \alpha_s(T_s - T_0)L_p$, w_n, w_s are the normal and shear separations of the Gauss point, α_c, α_s = thermal expansion coefficients of concrete and steel, respectively, T_s, T_c = temperatures for effective concrete section and longitudinal reinforcement, respectively,

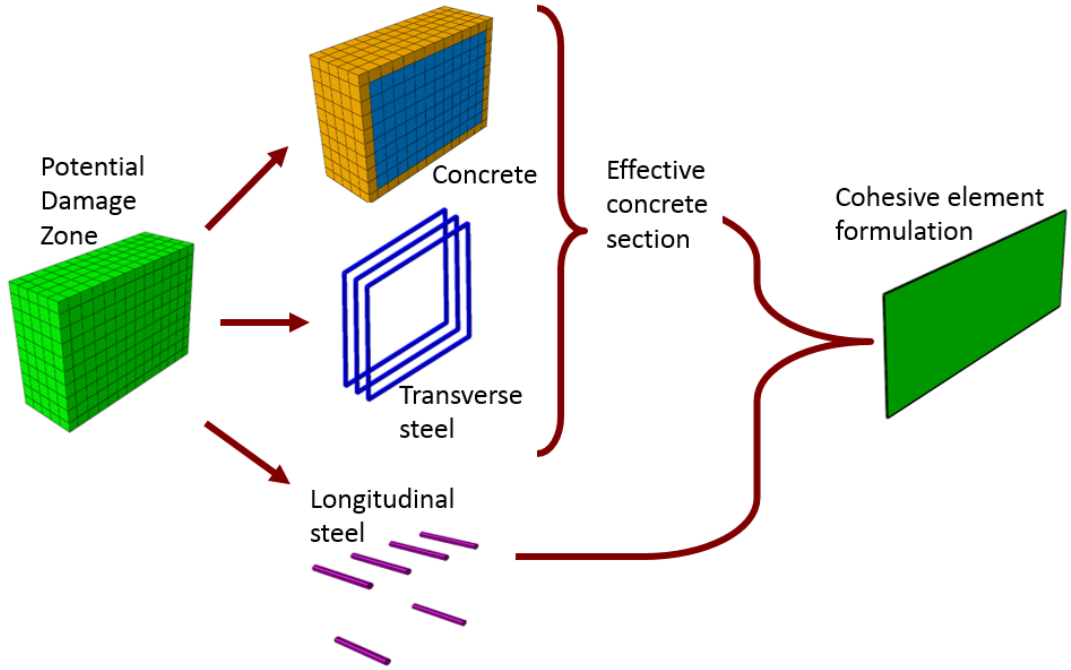

Figure 2.2: Components of the cohesive element model.

T_0 = room temperature, L_p = length of the potential damage zone and ρ_s is the longitudinal reinforcement ratio for the portion of the potential damage zone represented by the Gauss point.

2.1.1 Effective concrete section

For the effective concrete section, the interaction between normal and shear loading must be considered for the cohesive traction-separation relationship. In this study, we follow Le and Xue [27] in describing the mixed-mode constitutive behavior through the concept of effective traction and separation, adapted from recent modeling of cementitious materials [36].The effective separation is defined as $\bar{w} = \sqrt{w_{nt}^2 + \zeta_i^2 w_s^2}$ and the mode mixity angle as $\theta = \tan^{-1}(w_{nt}/|\zeta_i w_s|)$ [37], where ζ_i are the constants corresponding to combined tensile-shear (for $i = t$) and combined compression-shear loading (for $i = c$). The effective traction $\bar{\sigma}$ is work-conjugate to the effective separation $\bar{w}$, and

must satisfy the principle of virtual work in Eq. 2.3:

$$\bar{\sigma}\delta\bar{w} = \sigma_n^c \delta w_{nt} + \tau^c \delta w_s \tag{2.3}$$

Substituting $\bar{w}$ into Eq. 2.3 gives: $\bar{\sigma}\sin\theta\delta w_{nt} + \zeta_i\bar{\sigma}\cos\theta\delta w_s = \sigma_n^c\delta w_{nt} + \tau^c\delta w_s$. Since this equation has to be valid for any arbitrary values of δw_{nt} and δw_s, we obtain: $\sigma_n^c = \bar{\sigma}\sin\theta$ and $\tau^c = \zeta_i\bar{\sigma}\cos\theta$. From this it is clear only the traction-separation law in $\bar{\sigma} - \bar{w}$ space needs to determined, and from this the corresponding normal and shear cohesive tractions can be calculated.

The effective traction and separation are work-conjugate, making the area under the $\bar{\sigma} - \bar{w}$ curve represent the total energy dissipation of the failure of the effective concrete section. Since it is known that the collapse behavior of structural components is governed by the total energy dissipation capacity [38, 39, 40, 41, 42], the detailed shape of the softening branch is not crucial for modeling of structural systems. For this reason, a linear softening behavior can be assumed without significant loss of accuracy. For this model, $\bar{\sigma}(\bar{w})$ can be written as

$$\bar{\sigma}(\bar{w}) = \begin{cases} \sigma_p\bar{w}/\bar{w}_y & (\bar{w} \le \bar{w}_y) \\ \sigma_p(\bar{w}_u - \bar{w})/(\bar{w}_u - \bar{w}_y) & (\bar{w}_y < \bar{w} \le \bar{w}_u) \\ 0 & (\bar{w}_u < \bar{w}) \end{cases} \tag{2.4}$$

Here σ_p is the maximum effective traction, $\bar{w}_y$ is the effective separation at which σ_p is reached, and $\bar{w}_u$ is the ultimate effective separation at which the effective traction drops to zero. $\sigma_p, \bar{w}_y$ and $\bar{w}_u$ are calculated as

$$\sigma_p = |\sigma_{ip}|\sin^{\beta_i}|\theta| + \zeta_i^{-1}|\sigma_{\tau p}|\cos^{\beta_i}|\theta| \tag{2.5}$$

$$\bar{w}_y = [(|w_{iy}|\sin|\theta|)^{\gamma_i} + (|w_{\tau y}|\cos|\theta|)^{\gamma_i}]^{1/\gamma_i} \tag{2.6}$$

$$\bar{w}_u = [(|w_{iu}|\sin|\theta|)^{\gamma_i} + (|w_{\tau u}|\cos|\theta|)^{\gamma_i}]^{1/\gamma_i} \tag{2.7}$$

where σ_{ip} are the tensile ($i = t$) and compressive ($i = c$) strengths of the effective concrete section, $\sigma_{\tau p}$ is the shear strength of the effective concrete section, w_{iy} are the separations at which the cohesive traction reaches σ_{ip} under pure tensile and compressive loading, w_{iu} are the separations at which the cohesive traction drops to zero under pure tensile and compressive loading, $w_{\tau y}, w_{\tau u}$ are the separations at which the shear stress

reaches $\sigma_{\tau p}$ and zero, respectively, if the cohesive element is purely loaded in shear, and $\zeta_i, \beta_i, \gamma_i$ are calibration constants. This formulation simplifies to the normal or shear traction-separation relationship for single-mode loading, which also is assumed to have a linear softening behavior. Fig. 2.3 shows the interaction between the normal and shear cohesive behaviors. This model is able to capture the difference in fracture energies under normal, shear, and multi-axial loading. This formulation differs from the conventional cohesive laws, which are limited to tensile and shear failure, by including compressive failure, a necessary mechanism in beam and column failure. Compressive failure is included by allowing a small negative cohesive separation.

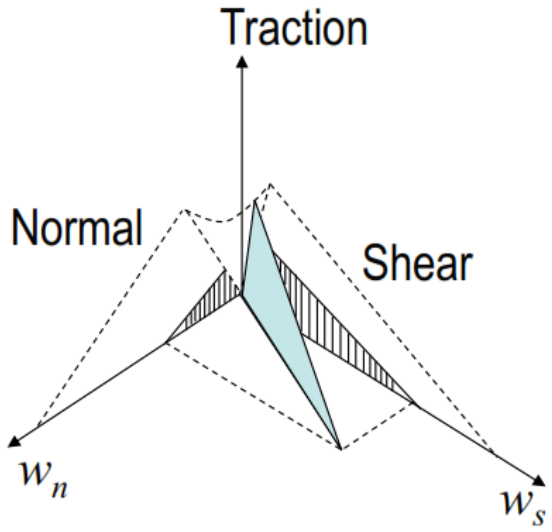

Figure 2.3: Interaction between normal and shear cohesive behavior.

During the collapse process, the structural components often experience some oscillation. It is expected that the amplitude of the oscillation is not large due to damping and therefore the failure of the structural components is mainly governed by the monotonic cohesive behavior. Yet some simple representations of unloading and reloading behavior for the cohesive elements must be included. For the effective concrete section, the unloading and reloading behaviors are described in the effective traction-separation space. The unloading and reloading paths are enclosed by the monotonic $\bar{\sigma} - \bar{w}$ curve given by Eq. 2.4. Within this envelope, the unloading-reloading path can be written

as:

$$\delta\bar{\sigma} = \bar{E}(1-\omega)\delta\bar{w} \tag{2.8}$$

where $\delta\bar{\sigma}, \delta\bar{w}$ are the incremental effective traction and separation, $\bar{E} = \sigma_p/\bar{w}_y$ is the undamaged elastic modulus, and ω is a damage parameter, which represents the maximum damage extent that the cohesive element has ever experienced during the loading history. For this study, we write ω as:

$$\omega = \min\left(\frac{\max_t\left[(1-E_p/\bar{E})h(\theta)\right]}{h(\theta)}, 1\right) \tag{2.9}$$

where $\max_t(x)$ is the maximum value of x during the loading history, $E_p = \bar{\sigma}/\bar{w}$ is the secant modulus, and $h(\theta)$ is a function relating the effect of the existing damage on the current material behavior to a change in the degree of mode mixity. In this study, it is assumed that $h(\theta) = 0.6 - 0.4\sin\theta$ for the sake of simplicity, and since it is expected that the mode mixity does not change significantly during the oscillation.

2.1.2 Longitudinal reinforcement

For the longitudinal reinforcement cohesive tractions,σ_n^s and τ^s, the bond-slip effect needs to be considered. Following a recent study by Lew et al. [43],the bond-slip effect is taken into account by modifying the uniaxial stress-strain relationship of the steel reinforcement, where the total normal strain ϵ in the reinforcement can be written as:

$$\epsilon(\sigma) = \epsilon_0(\sigma) + \Delta_s/L_p \tag{2.10}$$

where σ is the normal stress of the reinforcement, $\epsilon_0(\sigma)$ is the normal strain of the reinforcement without considering the bond-slip effect, Δ_s is the total slip of the reinforcement. The total reinforcement slip Δ_s is calculated from the bar stress using an analytical model from Sezen and Moehle [44], which assumes two piecewise constant segments based on the normal strain ϵ_0 for the bond stress profile, and a bi-linear hardening behavior for the stress-strain relationship of the steel reinforcement (for a detailed description, see [44]).

The ultimate value of the bar stress, F_u, is governed by two failure modes: bar rupture and bar pullout. For bar rupture, F_u is equal to the ultimate strength of the steel reinforcement. For bar pullout, F_u can be calculated based on the recommendation of

ACI [45]. This gives a simple stress-strain relation for reinforcement $\sigma = f(\epsilon)$, taking into account the bond-slip effect. This approach is similar to an analytical bond-slip model proposed for studying beam-column joints under seismic loading [34].

In a potential damage zone, the deformation of the longitudinal reinforcement is usu-

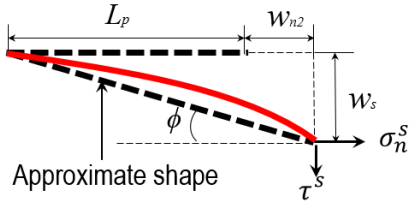

Figure 2.4: Normal and shear deformation of longitudinal reinforcement.

ally small, and the total elongation of the reinforcement, w can be approximated as $\sqrt{(L_p + w_{nt})^2 + w_s^2} - L_p$ (see Fig. 2.4). Based on the modified stress-strain relationship of the steel reinforcement, the corresponding normal and shear stresses can be calculated as $\sigma_n^s = f(w/L_p)\cos\phi$, and $\tau^s = f(w/L_p)\sin\phi$. Here, ϕ is the slope of the deformed reinforcement. In most cases, ϕ is small, and the longitudinal reinforcement contributes little to the shear cohesive resistance.

For the unloading and reloading of the longitudinal steel reinforcement, the responses are computed using the standard linear isotropic and kinematic strain hardening model [46]. This model assumes the unloading and reloading stiffnesses are equal to the initial elastic modulus, and the paths remain enclosed by the monotonic effective traction-separation curve. Fig. 2.5 presents the unloading and reloading curves for the effective concrete and longitudinal steel reinforcement.

2.2 Modeling of Thermo-Dependent Cohesive Behavior

2.2.1 Incorporation of temperature-dependent cohesive behavior

It has been well known that, besides the thermal expansion, the mechanical properties of concrete and steel reinforcement are strongly dependent on the temperature. Such

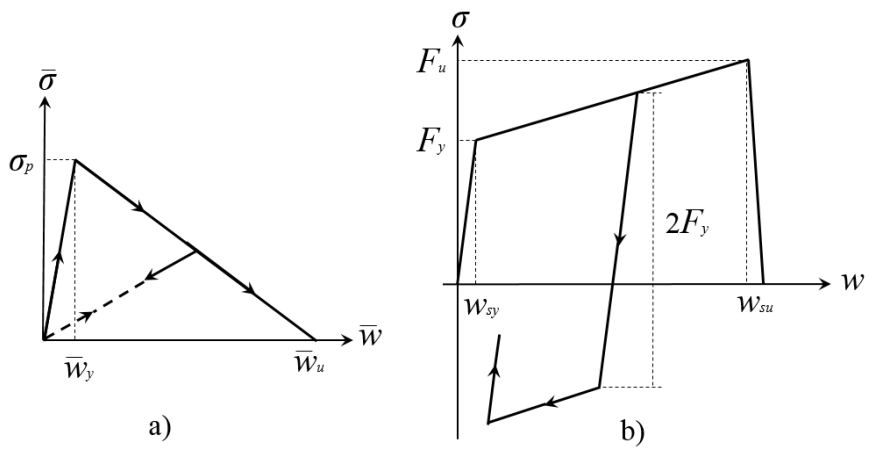

Figure 2.5: Loading and unloading behavior of cohesive element (a) effective concrete section and (b) longitudinal steel.

thermo-dependence of the mechanical behavior is incorporated into the present model by considering that the constitutive properties are functions of temperature. For concrete, the relevant constitutive properties include the peak stresses, σ_{cp}, σ_{tp}, and $\sigma_{\tau p}$, the corresponding separation w_{ty}, w_{cy}, and $w_{\tau y}$, and the energy dissipation in each direction, which are used to calculate the maximum separations at failure, w_{tu}, w_{cu}, and $w_{\tau u}$. Here it is assumed that the parameters governing the mode-mixity interaction, ζ_t and ζ_c, are independent of temperature. For the longitudinal steel, the temperature dependent parameters are the elastic modulus, and the yield and the ultimate strengths of the steel reinforcement. The ultimate strain at failure is assumed to be independent of temperature based on the recommendations of the Eurocode 2 [47]. Because there is a lack of data on the effect of temperature on the bond-slip behavior, it is assumed to be temperature-independent in the present model.

2.2.2 Spatial averaging of temperature field

To use the proposed cohesive model for RC frame structures under general thermomechanical loading, it is important to obtain the correct temperature for the Gauss points of the cohesive element. In the present model, each Gauss point of the cohesive element represents half of the potential damage zone. Two temperature values are used to obtain the constitutive behavior of each Gauss point: one for the effective concrete section T_c

and the other one for the longitudinal steel T_s.

To calculate these temperatures, we first need to perform a thermal analysis for the structural element for the given thermo-loading, from which the temperature distribution in the cross-section can be determined. For each Gauss point, the temperature input T_s for the longitudinal steel is simply the temperature occurring at the location of the longitudinal steel. By contrast, the temperature input T_c into the effective concrete section is somewhat more complex, where we need to use a single temperature input that can produce the actual behavior of the effective concrete section with a non-uniform temperature distribution. To get this representative temperature, a weighted average of the temperature through the half-section represented by each Gauss point is taken. The simplest approach is to average the temperature field that excludes the temperatures in the concrete cover. Such a simplification is expected to be sufficient for the present purpose because 1) the concrete cover does not contribute significantly to the flexural and shear resistances of the cross-section, which govern the frame behavior, and 2) the temperature gradient in the bulk part of the concrete cross section is not very steep due to its low thermal conductivity . This weighting procedure will be further discussed in the push-down test of a subassembly of structural elements in Chapter 5.

2.3 Outline of Model Calibration Procedure

It is evident that the proposed thermo-dependent cohesive model is phenomenological in nature, and therefore model calibration is essential. The cohesive elements explicitly represent the nonlinear behavior of the potential damage zones; therefore, it is proposed to use fine-scale nonlinear simulations to obtain the temperature-dependent mechanical behavior of the potential damage zones. The results of these fine-scale simulations can then be used to inform the constitutive properties of the cohesive elements. While many sophisticated numerical models can be used for the fine-scale simulations, in this study a finite element (FE) model is implemented since it allows direct input of material parameters which can be tested in a laboratory. This eliminates the need to calibrate the material behavior of the fine-scale model to match material tests. Using the separation of parts shown in Equations 2.1 and 2.2, the constitutive behavior of the effective concrete section is calibrated apart from the longitudinal reinforcement.

The effective concrete section is calibrated by performing FE simulations of the potential damage zone under various loading modes. At room temperature, the modes include tension, compression, and shear, as well as combined tension-shear and compression-shear, to determine the mode mixity parameters ζ_i, β_i and γ_i for tension($i = t$) and compression ($i = c$). At temperatures above room temperature, single loading modes are tested at a uniform temperature to develop the temperature-dependence of the controlling parameters.

In order to run the fine-scale analysis, the size of the potential damage zone must be determined. Based on previous experimental observations [48], the length of the potential damage zones in concrete beams and columns L_p is about $0.5D$, where D is the full beam or column depth. For the beam-column joint panels, L_p is given by the diagonal crack band, which is approximately equal to $0.47L_d$ (L_d is the diagonal length of the panel) based on the compressive strut-and-tie model [49, 50]. The constitutive behavior of concrete is described by the damage plasticity model [51], where the finite element size should be chosen to equal to the crack band width in order to avoid the issue of spurious mesh sensitivity [31]. The transverse reinforcement is modeled by a set of truss elements with a bilinear elasto-plastic hardening behavior. The detailed model calibration process for the frame assemblage considered in this study will be presented in Chapter 4.

Chapter 3

Determination of Temperature-Dependent Material Properties

To calibrate the proposed thermo-dependent cohesive model, the fine-scale simulations of potential damage zones must involve the temperature-dependent material properties of steel and concrete. In this research, the temperature-dependent material properties of steel are determined from the well-established literature data, whereas for concrete the temperature-dependent material properties are determined from a combination of high-temperature experiments and existing literature. Based on the typical constitutive models of steel and concrete, the controlling material properties for steel are the elastic modulus and the yield and ultimate strengths, and for concrete, the critical material properties are the elastic modulus, the tensile and compressive strength, and the fracture energy densities in both tension and compression.

3.1 Steel Properties

Properties of steel at high temperature have been extensively studied for steel members [52, 53, 54] and as reinforcement in concrete [55, 56]. In this study, we consider that the temperature dependence of steel properties follows the recommendation of the Eurocode

2 [47]. The steel yield strength σ_y, ultimate strength σ_u, and elastic modulus E_s are all modified from their room-temperature values using tabulated ratios, as shown in Table 3.1.

	Ratio to Value at Room Temperature		
Temperature	Ultimate Stress	Yield Stress	Elastic Modulus
20	1	1	1
100	1	1	1
200	1	0.81	0.9
300	1	0.61	0.8
400	1	0.42	0.7
500	0.78	0.36	0.6
600	0.47	0.18	0.31
700	0.23	0.07	0.13
800	0.11	0.05	0.09
900	0.06	0.04	0.07
1000	0.04	0.02	0.04
1100	0.02	0.01	0.02
1200	0	0	0

Table 3.1: Temperature dependence of steel material properties from Eurocode 2 [47].

3.2 Concrete Properties

A large number of empirical and semi-empirical models have been proposed in the literature for concrete material properties subject to high temperature [15, 57, 58, 59, 17, 56]. The existing models vary significantly from each other as they were developed and fitted for some specific mix designs. Therefore, in this research, we test a specific concrete mix design, and the measured temperature-dependent material properties are then used for the latter numerical simulations, as will be described in Chapters 4 and 5. It should be pointed out that the present experiments are focused on the compressive behavior since the tensile behavior of RC frame structural components is mainly governed by the steel reinforcement.

The experiment was performed at the National University of Singapore (NUS) in the Department of Civil and Envirnmental Engineering. The concrete was prepared in three batches on three consecutive days, using the mix design shown in Table 3.2.

(a) (b)

Figure 3.1: Furnace for heating specimens; (a) front of furnace, and (b) one specimen from each of three batches are heated together.

The concrete was poured into 100mm x 200mm cylinder forms and cured in a fog room with controlled temperature and humidity for 28 days. 10 different temperatures were considered in the tests. For each temperature tested, one cylinder from each batch was put into a furnace (shown in Fig. 3.1) and heated at a rate of 5°C per minute until the desired temperature was reached. The cylinders were then left at the temperature for 2.5 hours to assure uniform heating, then allowed to cool to room temperature for the mechanical loading. This procedure is a residual property test, and results differ from the in situ properties, but the difference can be reduced by the method of cooling chosen [60].Quick cooling methods such as using a water bath can cause excess damage to the concrete beyond the fire damage, while exposure to moisture during cooling can allow compounds broken down at high temperature to rehydrate [60]. To prevent excess damage and rehydration, the cylinders were cooled within the closed furnace and then kept in a tightly sealed container until testing.

A displacement-controlled compression test was performed on the cylinders (see Fig. 3.2), where the applied force and relative displacement were recorded. The cylinders were tested beyond peak strength into the softening branch to get an approximate measurement of total energy released in compression failure. The test results were then transformed into stress-strain relations using the measured dimensions of the concrete

Concrete Mix Components kg/(m^3 concrete)	
water	180
cement	425
sand	810
coarse aggregate	950

Table 3.2: Concrete Mix Design used for Testing

Figure 3.2: Cylinder compression test.

cylinders, and are shown in Fig. 3.3. The key properties of compression strength, elastic modulus, and fracture energy density were then extracted and compared to the literature.

The peak compression stress, following the model in the Eurocode 2 [47], is assumed to decrease as

$$\frac{f_c'(T)}{f_{c0}'} = \begin{cases} 1 & T \leq 100°\text{C} \\ 1.067 - 0.00067T & 100°\text{C} < T \leq 400°\text{C} \\ 1.44 - 0.0016T \geq 0 & T > 400°\text{C} \end{cases} \tag{3.1}$$

The experimental data is reasonably consistent with this model as shown in Fig. 3.4. It is notable that the concrete strength appears to decrease somewhat at the boiling point of water and increase beyond the initial strength at temperatures close to 300°C. This has been observed in the literature, and it was argued that it could be due to the residual test procedure. This point would need to be verified by in situ testing

of concrete [61, 60]. On the other hand, no existing models proposed in the literature consider the rise in material strength at moderately high temperature. Based on Fig.3.4, the Eurocode 2 model is considered sufficiently conservative for the tested concrete.

The temperature dependence of concrete elastic modulus is considered to follow the model proposed by Lee et al. [57] based on the experimental results. This model is selected because it was developed based on the chemical changes undergone within the concrete due to heating. The comparison of the test data, the original model and the modified model are shown in Fig. 3.5. The resulting formula for the elastic modulus can be written as the product of two functions, and the original elastic modulus $E_c(T) = d_a(T)d_c(T)E_{c0}$. These two functions are given in Eqs. 3.2 and 3.3.

$$d_a(T) = 0.00896 + \exp(-0.0003 \times T) \tag{3.2}$$

$$d_c(T) = \begin{cases} \dfrac{3431.2 - 3.32 \times T}{2740 + T} & 20°\text{C} \leq T \leq 400°\text{C} \\ \dfrac{10(675 - T)(3431.2 - 3.32 \times T)}{8435000 + 100 \times T + T^2} & 400°\text{C} < T < 550°\text{C} \\ 0.467728177 \times \dfrac{3431.2 - 3.32 \times T}{2740 + T} & 550°\text{C} \leq T \end{cases} \tag{3.3}$$

The fracture energy density of concrete in compression is not as well studied as other material properties. However, this is a critical material property that governs the failure behavior of the structural components. To develop a model for the compression energy, in situ compression tests reported graphically in the literature [62, 63, 64] are collected and the fracture energy densities under the stress-strain curves are extracted. A simple piece-wise linear function is fitted to the data, as the scatter of data is too large for a more accurate fit. The general behavior of concrete at high temperature is observed to be a decrease in strength, elastic modulus, and an increase in ductility. This combination results in little or no loss of energy dissipation capacity at moderately high temperatures (up to 600 °C), after which a steep decline in energy dissipation capacity occurs. A similar trend is found in the results from the residual tests performed at NUS. Combining the results specific to the tested concrete and those observed in the literature, an approximate relationship is established, and shown in Eq. 3.4.

$$\frac{\gamma_c(T)}{\gamma_{c0}} = \min\left[, 2.7048 - 0.0029T\right] \tag{3.4}$$

This approximation can be seen along with the literature and test data in Fig. 3.6.

As mentioned, the performance of the concrete under tensile loading was not tested in the laboratory since the tensile behavior of concrete does not affect significantly the global behavior of RC frame structures. In this study, the temperature-dependent tensile properties of concrete are determined based on the existing literature. Based on the American Concrete Institute (ACI) Code 318 [65], the tensile strength at room temperature is approximated as $6.7\sqrt{f'_{c0}}$ where the room temperature compression and tension strengths are both in pounds per square inch. The compressive strength at room temperature was measured in the aforementioned experiment. The model of peak tensile stress as a function of temperature is based on a model proposed by Bažant and Chern [15].

$$\frac{f'_t(T)}{f'_{t0}} = \begin{cases} 1.01052 - 0.000526T & 20°\text{C} \leq T \leq 400°\text{C} \\ 1.8 - 0.0025T & 400°\text{C} < T \leq 600°\text{C} \\ 0.6 - 0.0005T & 600°\text{C} < T \leq 1000°\text{C} \end{cases} \tag{3.5}$$

The fracture energy density of concrete in tension is assumed to decrease with temperature following a formula given by Bažant and Prat[66]. This function is plotted along with the tensile strength reduction factor in Fig. 3.7.

$$\frac{G_f(T)}{G_{f0}} = \exp\left(\frac{600}{T+273} - \frac{600}{293}\right) \tag{3.6}$$

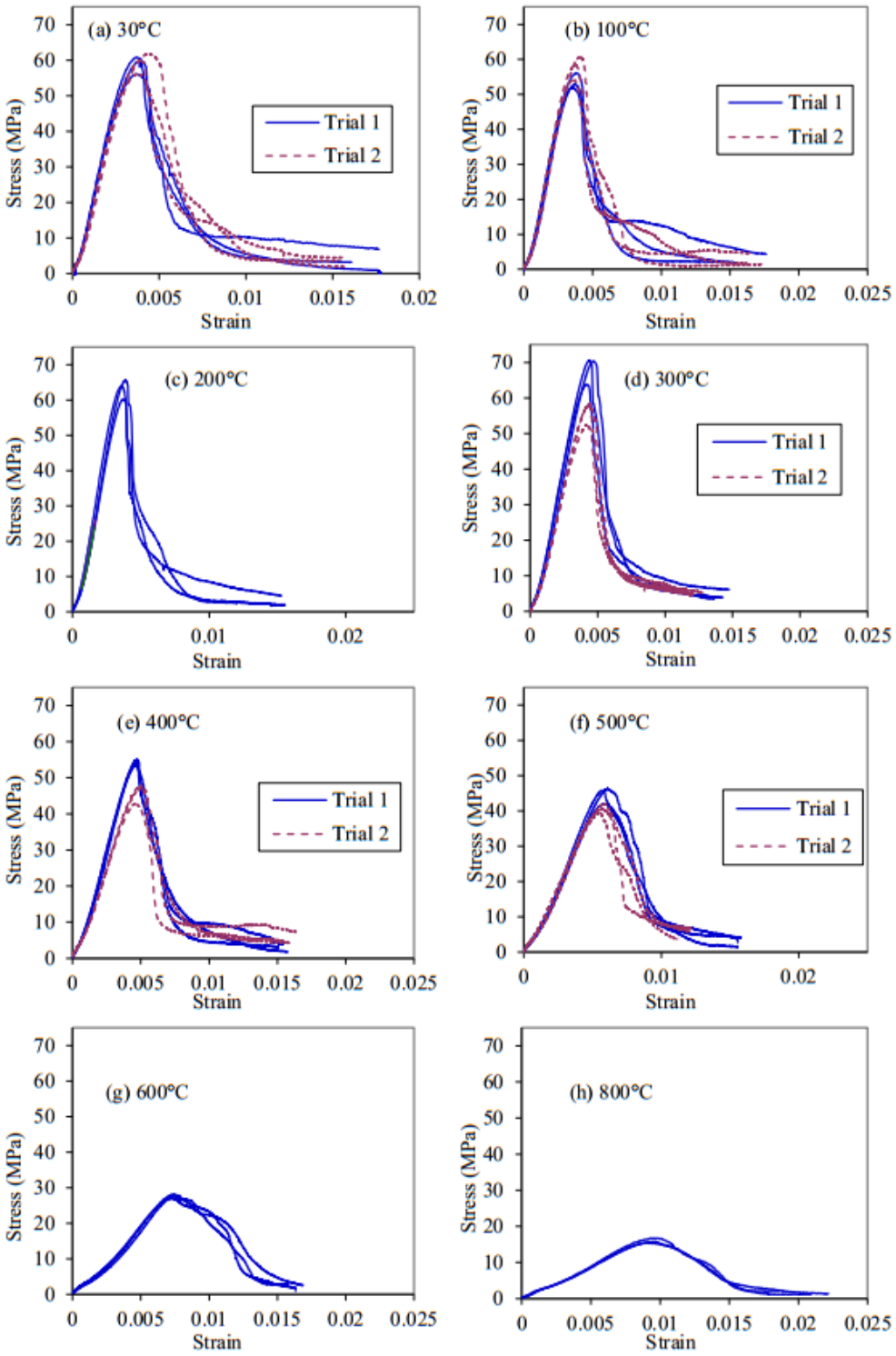

Figure 3.3: Measure compressive stress-strain curves of concrete at different temperatures.

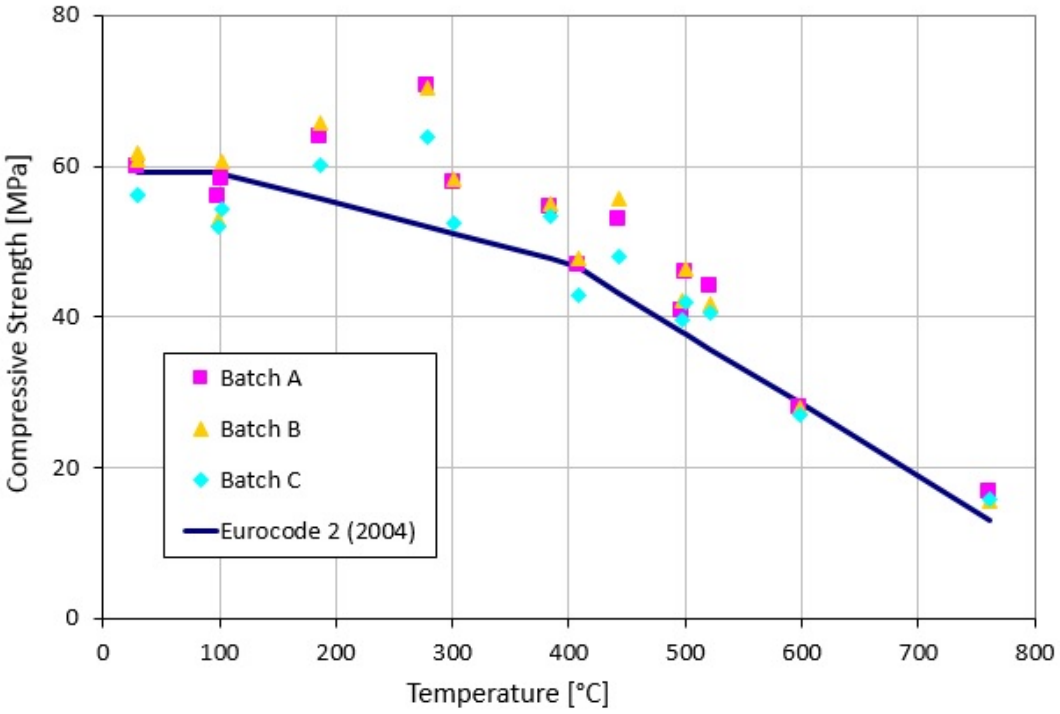

Figure 3.4: Compression strength of concrete versus temperature.

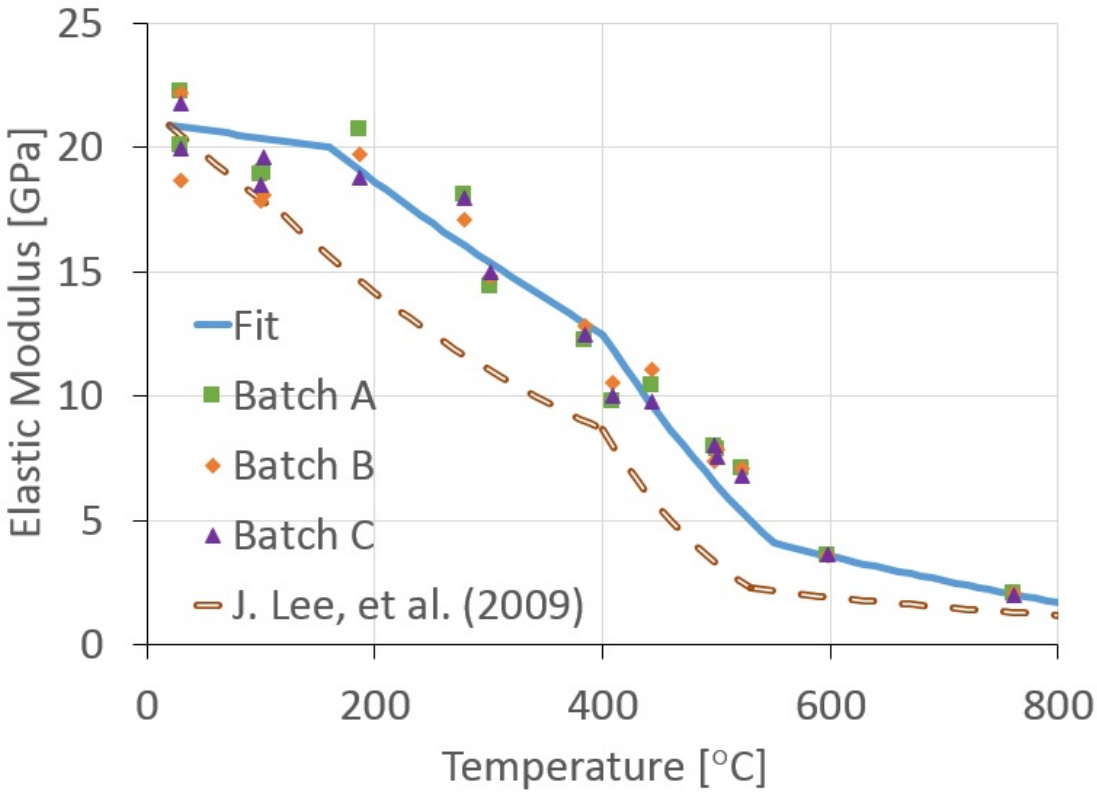

Figure 3.5: Elastic modulus of concrete versus temperature.

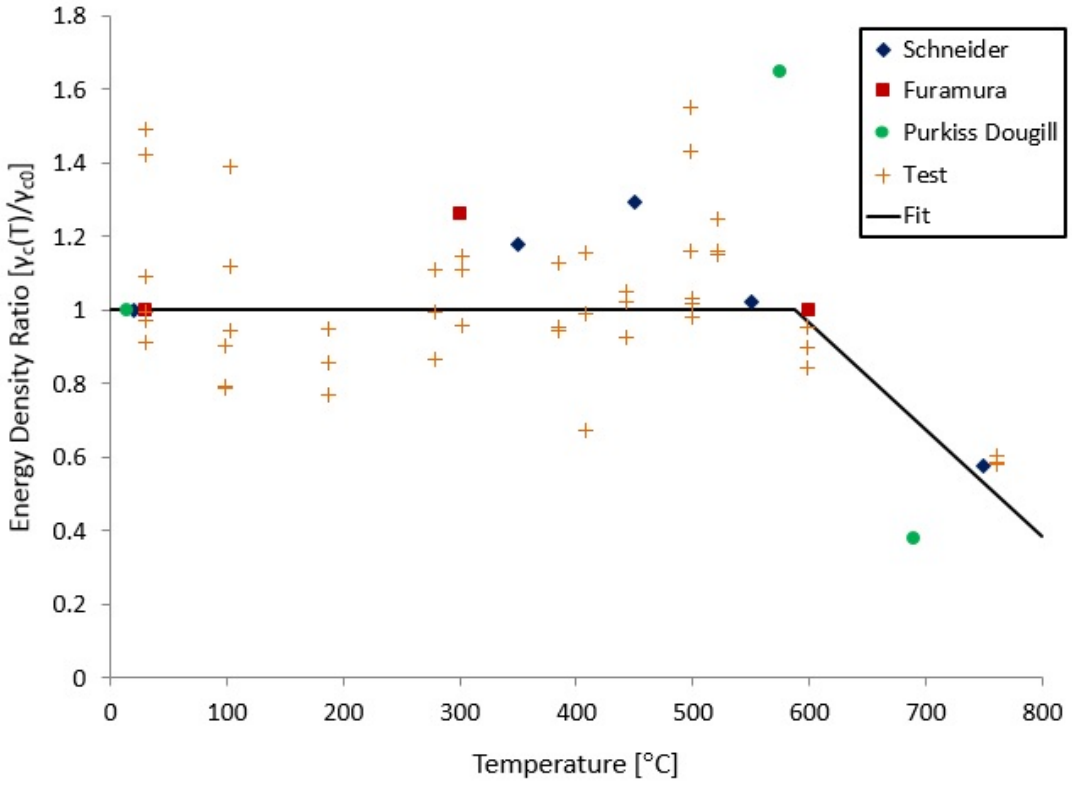

Figure 3.6: Compression energy density for cylinder tests compared to the literature [62, 63, 64].

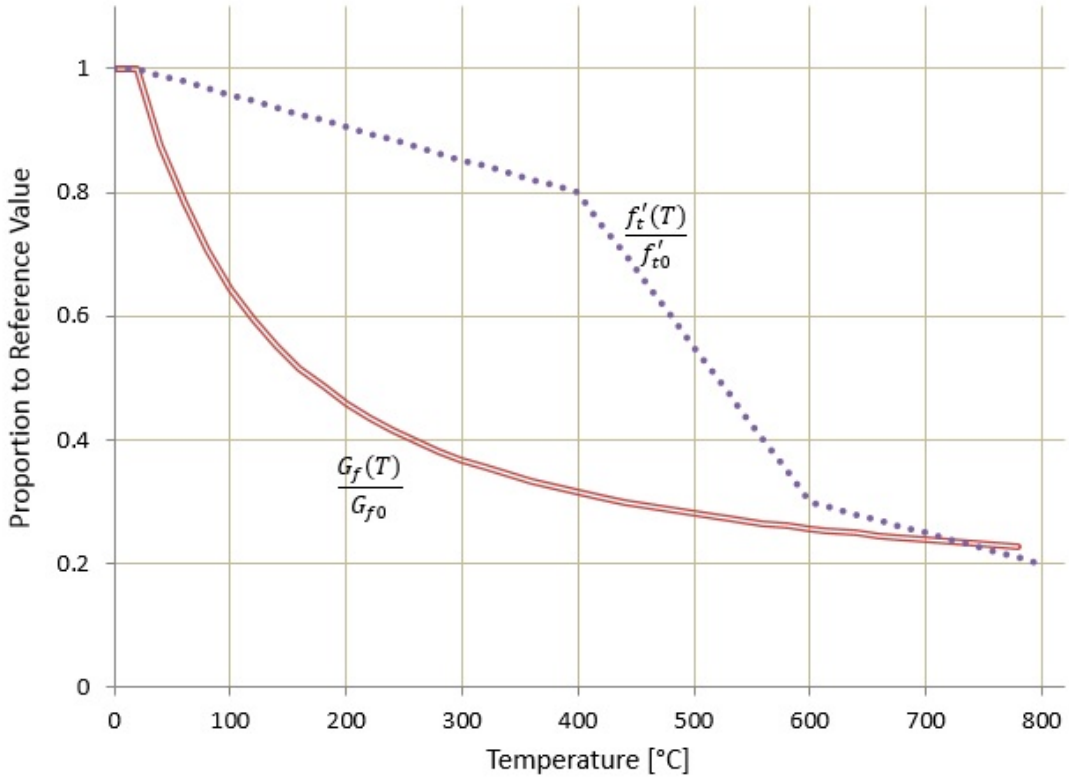

Figure 3.7: Tension properties of concrete versus temperature.

Chapter 4

Finite Element Based Calibration of Cohesive Model

Once the temperature-dependence of various material properties of concrete and steel is determined, fine-scale FE simulations are performed to determine the thermo-dependent constitutive properties of the cohesive element for each potential damage zone. Based on the formulation of the cohesive element model, the FE simulations involve the determination of the entire load-deflection curve of the potential damage zone under pure tension, compression and shear at different temperatures, and empirical equations are proposed to fit the simulated temperature dependence of strengths and energy dissipations under these loading modes, which can directly be input into the proposed cohesive element model.

4.1 Description of Fine-Scale FE Simulations

We demonstrate the fine-scale FE-based calibration of the cohesive elements by considering a RC frame subassemblage shown in Fig. 4.1. The design of this frame is according to a recent full-scale experiment conducted by NIST[43] on the behavior of RC frame subassemblage under sudden column removal. In Chapter 5, we will use the calibrated cohesive element model to simulate the behavior of this frame subassemblage under thermomechanical modeling. As seen in Fig. 4.1, there are three potential damage zones that need to be considered: one at the beam center, one at the beam end,

and one in the column.

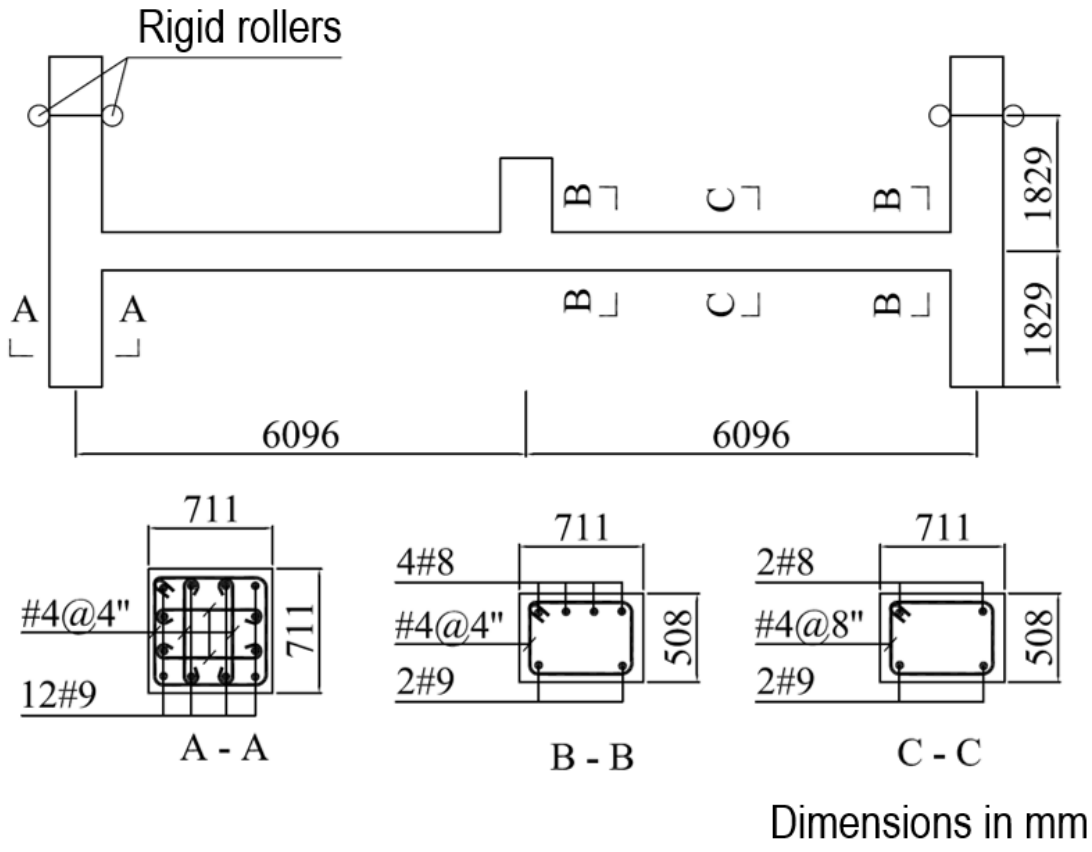

Figure 4.1: Structural layout for push-down test used to verify cohesive element model.

In the FE simulations, the length of the potential damage zone is considered to be half of the depth of the structural element for beams and columns, based on the experimental observations [48], i.e. $L_p = 250$ mm for the beam, and $L_p = 350$ mm for the column. For the joint panels, the width of potential damage zone should correspond to the diagonal crack band, which is about $0.47L_d$ (L_d = diagonal length of the joint), based on the strut-and-tie model [49, 50]. The constitutive behavior of concrete is described by the damage plasticity model [51], with a prescribed stress-strain behavior in tension and in compression, as well as an input unloading behavior. The finite element size is chosen to match the crack band width, which is approximately equal to 2 to 3 times the maximum aggregate size, so that we can avoid the issue of spurious

mesh sensitivity arisen from damage localization [31]. For the concrete mix design, the maximum aggregate size was 19 mm, giving a crack band width between 38 and 57 mm. 50 mm is chosen for the mesh size as it falls within the reasonable range. The transverse reinforcement as an elasto-plastic hardening material, described by a bilinear stress-strain curve. The transverse reinforcement is implemented in the FE model using a set of truss elements embedded in the continuum concrete model. Tables 4.1 and 4.2 show the constitutive properties of concrete and steel at room temperature, respectively, and the temperature dependence of these properties follows the empirical equations developed in Chapter 3.

Property	Value
Elastic Modulus	23000 MPa
Compression Peak Stress	59 MPa
Energy Dissipation in Compression	12500 N/m
Tension Peak Stress	4.3 MPa
Fracture Energy	80 N/m

Table 4.1: Constitutive properties of concrete at room temperature.

Property	Value
Elastic Modulus	120000 MPa
Yield Stress	414 MPa
Strain at Ultimate	0.29
Ultimate Stress	621 MPa

Table 4.2: Constitutive properties of steel at room temperature.

At room temperature, the single mode loadings are simulated (see Fig. 4.2) and the effective stress-strain curves are calculated from the force-displacement results. The bilinear function assumed for the effective concrete section cohesive element is then fit to capture the peak stress, corresponding strain, and energy dissipation of the potential damage zone. The constants that govern the mode mixity is assumed to follow the values obtained by Le and Xue [27], who studied the same frame subassemblage at room temperature. The mode mixity parameters ζ_i, β_i and γ_i for tension($i = t$) and compression ($i = c$) are given in Table 4.3.

At temperatures from 100°C up to 800°C, in increments of 100°C, single loading modes are tested at a uniform temperature to develop the temperature-dependence of

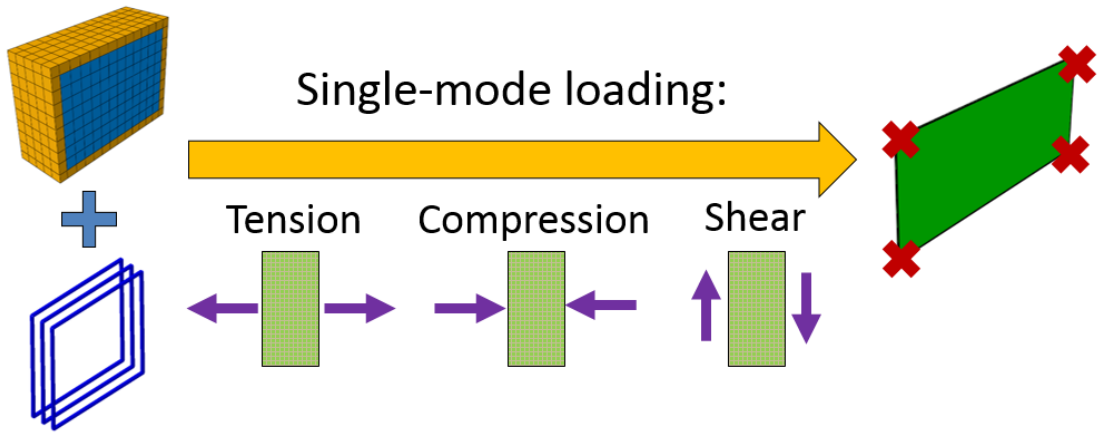

Figure 4.2: Illustration of loading scenarios modeled with FE simulations.

	Compression	Tension
ζ_i	0.53	0.3
β_i	2.25	1.0
γ_i	2	2

Table 4.3: Constants governing the mode mixity interaction.

the controlling parameters. Based on the averaged temperature input to the effective concrete section (described in Section 2.2) for the fire load used, 800°C is considered sufficiently high to prevent need of extrapolation (see Chapter 5 for more details on the fire load chosen). Each potential damage zone is loaded until failure in tension, compression, and shear, at each temperature, and the force-displacement curve is recorded. This is then converted into an effective stress-strain ($\sigma - \varepsilon$) curve for the zone. The force-displacement curves from the FE model are shown in Fig. 4.3 to 4.11. The stress-strain behavior of each simulation is then approximated by a linear ascending branch to capture the peak stress and corresponding strain, along with a descending branch that maintains the area under the $\sigma - \varepsilon$ curve. When implemented in the cohesive element formulation, this $\sigma - \varepsilon$ relation is transformed,using the length of the represented potential damage zone, into the $\sigma - w$ relation, and preserves the energy dissipation of failure of the effective concrete section. The key parameters of this cohesive relation are then plotted against temperature, and empirical equations are proposed to describe the evolution of each parameter with temperature, which can easily be implemented into

the proposed thermo-dependent cohesive model.

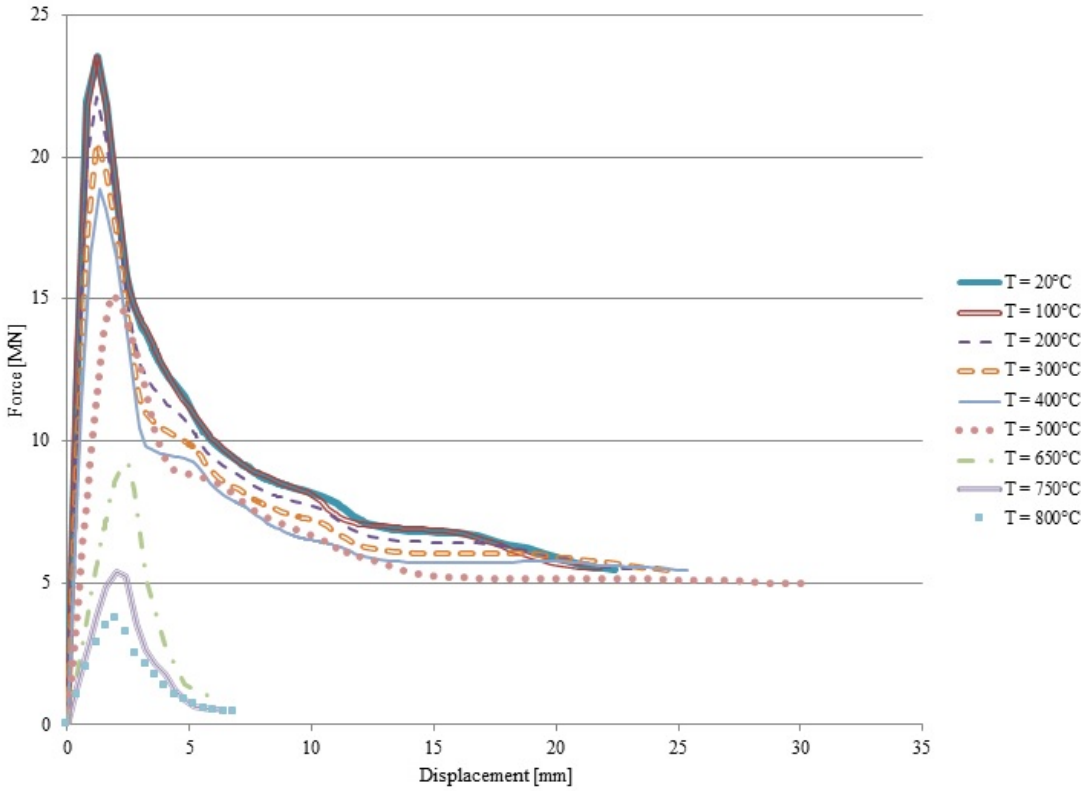

Figure 4.3: FE simulated force-displacement curve for compression of the beam end effective concrete section.

4.2 Calibration of Thermo-dependent Cohesive Properties for Effective Concrete Section

Based on the proposed cohesive element model, the key parameters of the simulated effective stress-strain curves for each loading mode include the strength, the critical strain at which the strength is reached, and the total fracture energy (i.e. the area under the effective stress-strain curve multiplied by the length of the potential damage zone). Figs. 4.12, 4.13, and 4.14 present the simulated temperature dependence of these

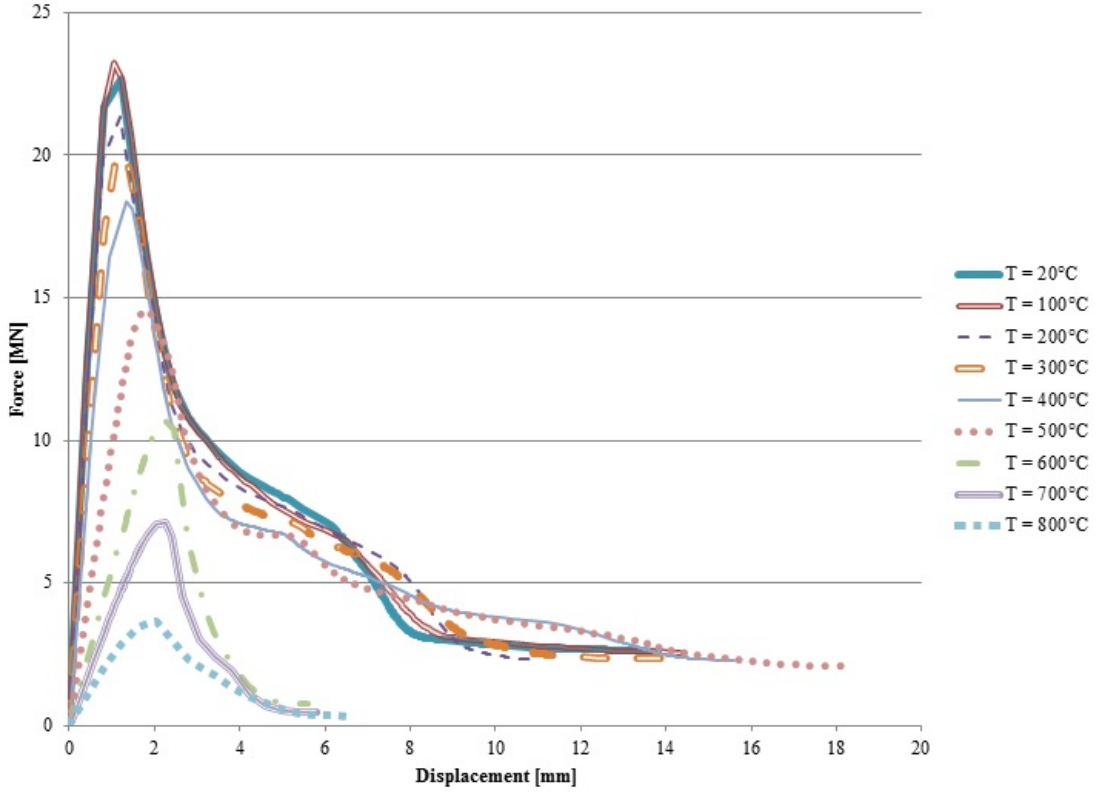

Figure 4.4: FE simulated force-displacement curve for compression of the beam centerline effective concrete section.

three parameters for compressive loading.

Based on the optimum fitting, the temperature dependent critical strain at which the compressive strength is reached can be described as:

$$\varepsilon_c'(T) = -1.76 \times 10^{-13} T^4 + 2.26 \times 10^{-10} T^3 - 7.37 \times 10^{-8} T^2 + 7.65 \times 10^{-6} T + 0.00424 \quad (4.1)$$

where ε_c' is the strain corresponding to the peak compressive stress, and T is the temperature across the damage zone in degrees Celsius. From Fig. 4.12, the critical strain remains relatively constant, then rises around 300 °C, but decreases after 650 °C. This complex behavior occurs due to the interaction between decreasing elastic modulus and simultaneous decreasing peak stress. There is little difference observed in the critical strain between the three different potential damage zones, which allows us to use a

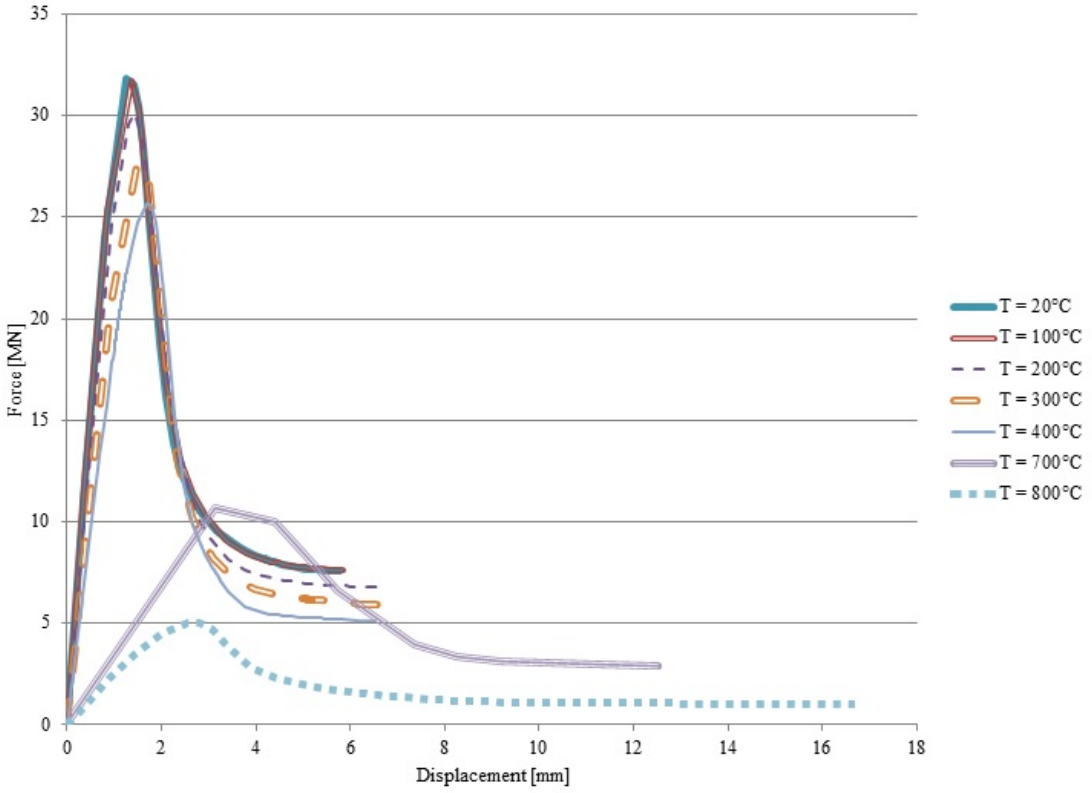

Figure 4.5: FE simulated force-displacement curve for compression of the column effective concrete section.

single equation for $\varepsilon_c'(T)$.

The optimum fits of the simulated compressive strength yields the following equation:

$$f_c' = 3.25 \times 10^{-10} T^4 - 4.40 \times 10^{-7} T^3 + 4.82 \times 10^{-5} T^2 - 0.0209T + 92.9 \qquad (4.2)$$

where f_c' is the peak compression stress in MPa, and T is in °C. In Fig. 4.13, the decrease in strength is monotonic, easily fit, and all of the potential damage zones exhibit the same trend. This is reasonable, since the main difference between the zones in compression is the amount of confinement of the concrete, which impacts the post-peak behavior.

The optimum fits of the simulated fracture energy density for all three potential

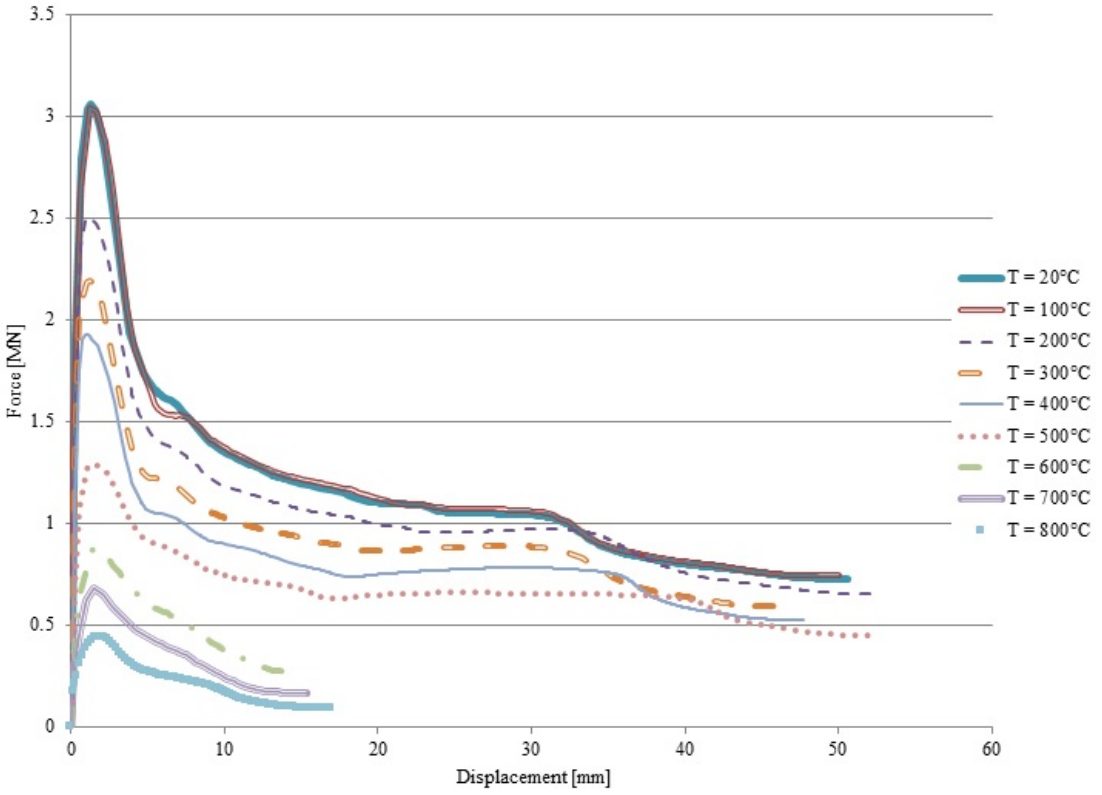

Figure 4.6: FE simulated force-displacement curve for shear of the beam end effective concrete section.

damage zones yields:

$$\gamma_{c1}(T) = \begin{cases} 3.156 & 20°\text{C} \leq T \leq 500°\text{C} \\ -0.02913T + 17.72 & 500°\text{C} < T \leq 600°\text{C} \\ 0.251\,[-0.0029T + 2.705] & 600°\text{C} < T \leq 800°\text{C} \end{cases} \tag{4.3}$$

$$\gamma_{c2}(T) = \begin{cases} 0.737 & 20°\text{C} \leq T \leq 500°\text{C} \\ -0.00495T + 3.21 & 500°\text{C} < T \leq 600°\text{C} \\ 0.251\,[-0.0029T + 2.705] & 600°\text{C} < T \leq 800°\text{C} \end{cases} \tag{4.4}$$

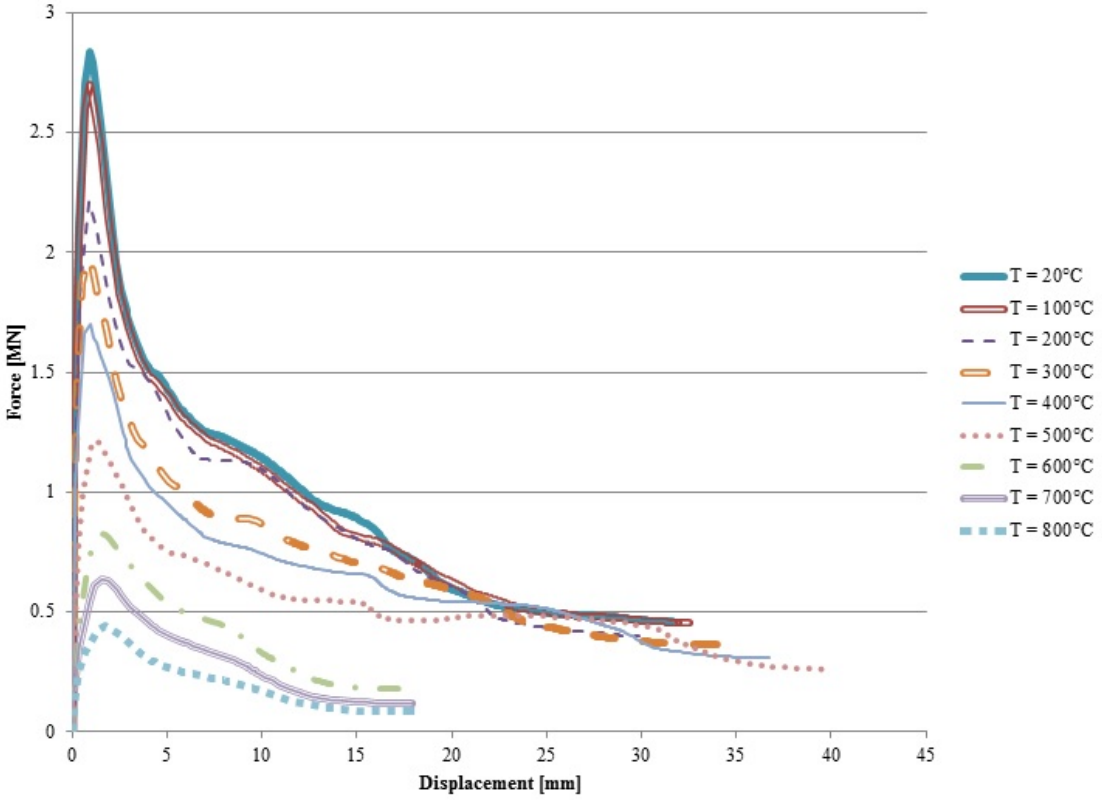

Figure 4.7: FE simulated force-displacement curve for shear of the beam centerline effective concrete section.

$$\gamma_{c3}(T) = \begin{cases} 0.621 & 20°\text{C} \leq T \leq 500°\text{C} \\ -0.0038T + 2.52 & 500°\text{C} < T \leq 600°\text{C} \\ 0.251\,[-0.0029T + 2.705] & 600°\text{C} < T \leq 800°\text{C} \end{cases} \tag{4.5}$$

where γ_{ci} is the compression energy density in MPa, T is in °C, and the subscripts (1, 2, 3) denote beam end section, beam center section, and column section, respectively. Based on Fig. 4.14, the energy dissipation of each potential damage zone differ significantly from each other for $T \leq 500°\text{C}$. This could be attributed to the fact that these three potential damage zone have very different transverse reinforcement ratios, which give different confinement effect on the concrete enclosed by the transverse reinforcement. For $T > 500°\text{C}$, it is expected that the transverse steel reinforcement starts

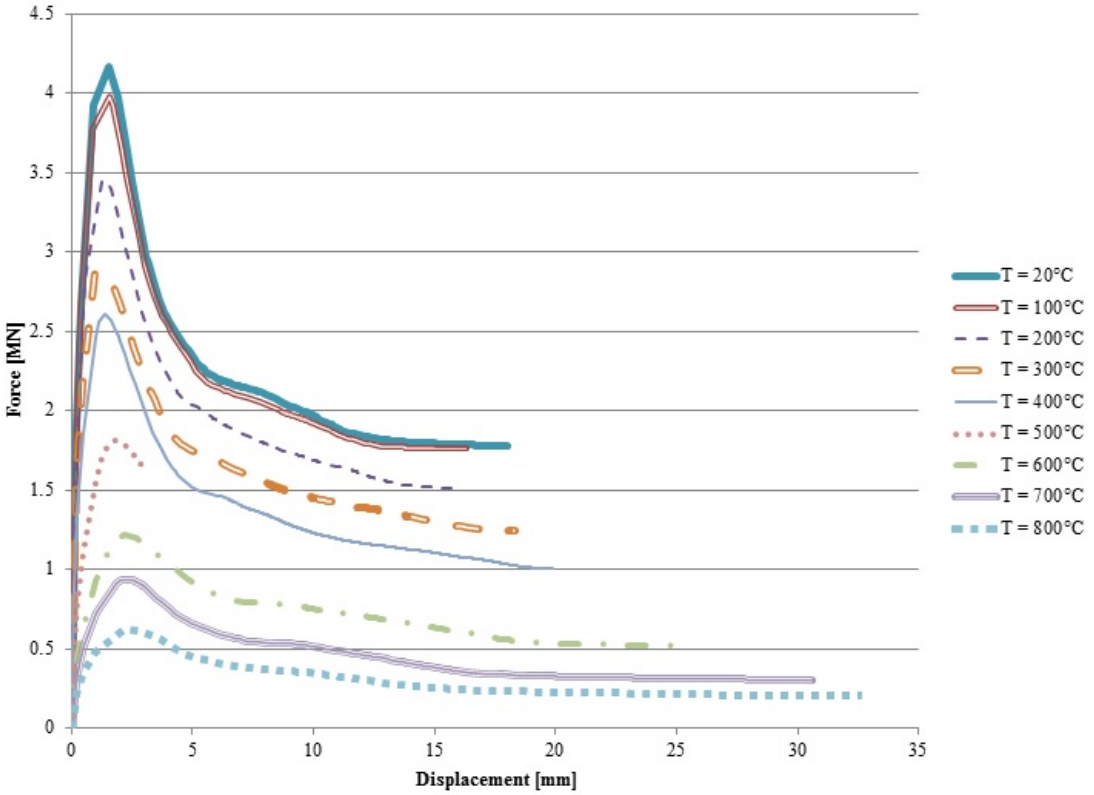

Figure 4.8: FE simulated force-displacement curve for shear of the column effective concrete section.

to lose a considerable amount of stiffness and strength, and therefore the confinement effect starts to diminish. This is clear from Fig. 4.14, which shows that the difference in total fracture energies among the three potential damage zones becomes much smaller as the temperature increases beyond 500°C.

Similarly, we use empirical equations to describe the simulated temperature-dependent critical strain, strength and fracture energy for pure shear loading, i.e.:

$$\varepsilon_v'(T) = -2.18 \times 10^{-11} T^3 + 3.58 \times 10^{-8} T^2 - 1.24 \times 10^{-5} T + 0.00496 \tag{4.6}$$

$$f_v'(T) = 2.30 \times 10^{-8} T^3 - 2.698 \times 10^{-5} T^2 - 0.00596 T + 12.02 \tag{4.7}$$

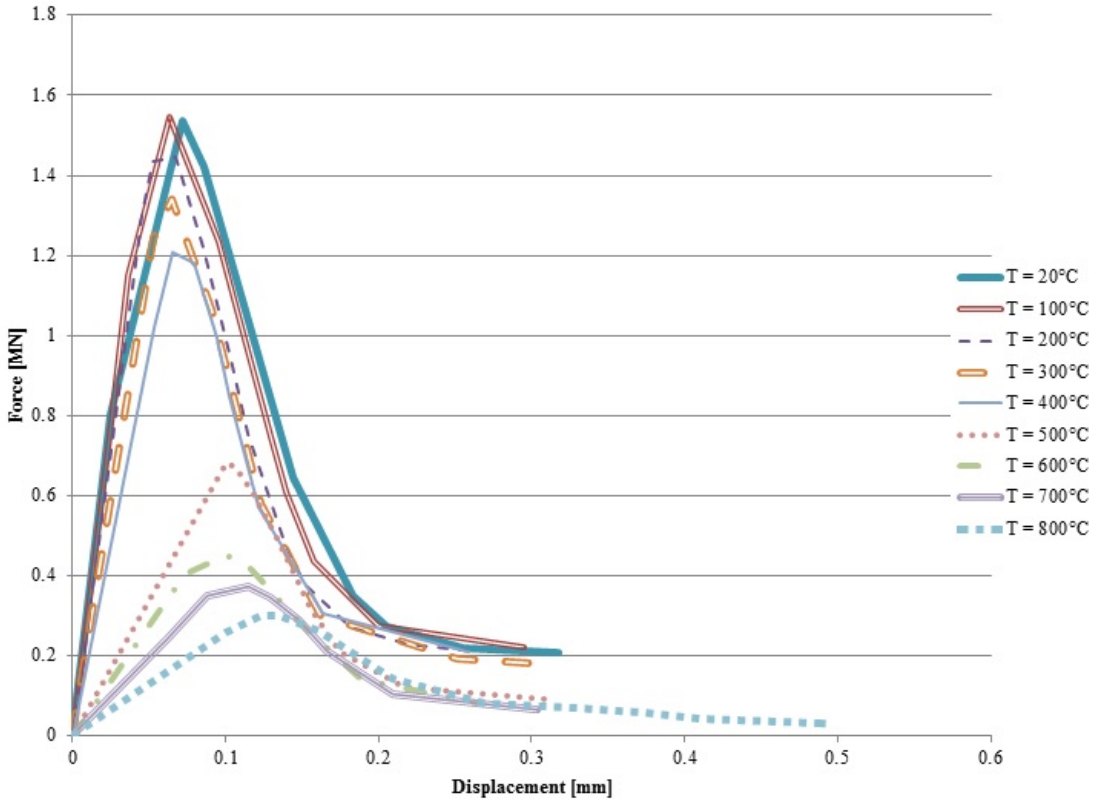

Figure 4.9: FE simulated force-displacement curve for tension of the beam end effective concrete section.

$$\gamma_{v1}(T) = \begin{cases} 0.9456 & 20°\text{C} \leq T \leq 100°\text{C} \\ 1.33 \times 10^{-6}T^2 - 0.001727T + 1.105 & 100°\text{C} < T \leq 500°\text{C} \\ -0.00447T + 2.809 & 500°\text{C} < T \leq 600°\text{C} \\ -3.15 \times 10^{-4}T + 0.316 & 600°\text{C} < T \leq 800°\text{C} \end{cases} \tag{4.8}$$

$$\gamma_{v2}(T) = \begin{cases} -3.13 \times 10^{-4}T + 0.501 & 20°\text{C} \leq T \leq 500°\text{C} \\ -0.00218T + 1.43 & 500°\text{C} < T \leq 600°\text{C} \\ -3.15 \times 10^{-4}T + 0.316 & 600°\text{C} < T \leq 800°\text{C} \end{cases} \tag{4.9}$$

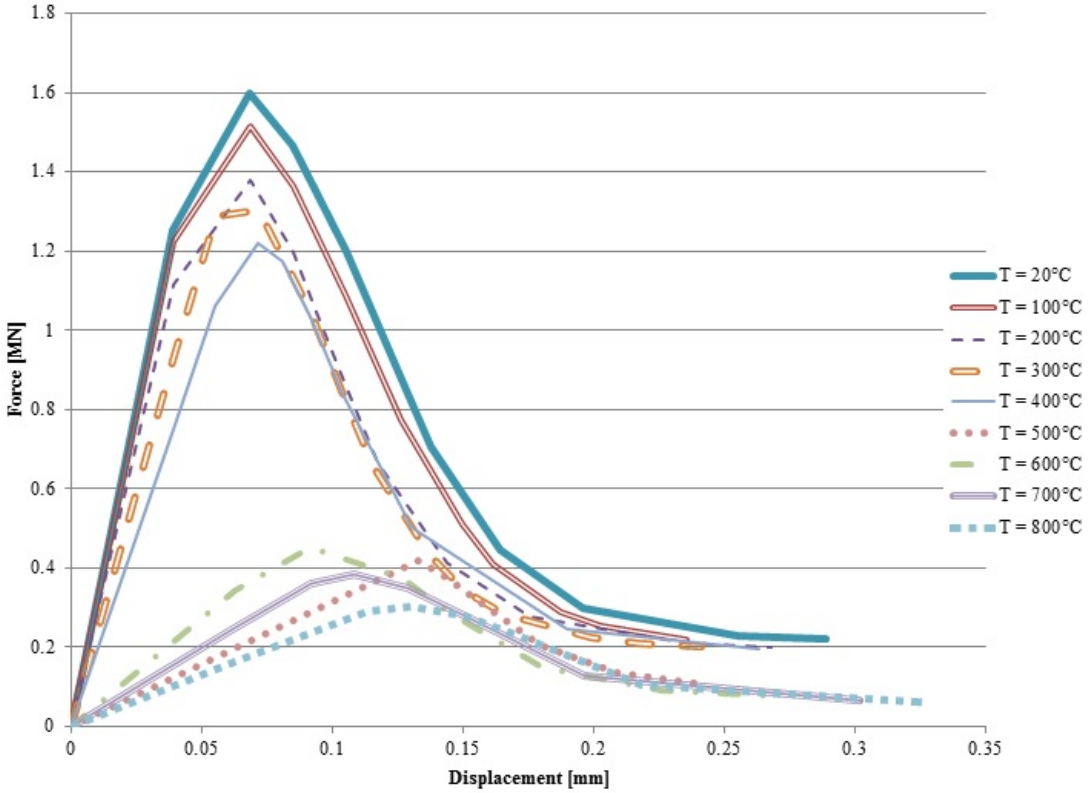

Figure 4.10: FE simulated force-displacement curve for tension of the beam centerline effective concrete section.

$$\gamma_{v3}(T) = \begin{cases} -0.00028(T) + 0.328 & 20°\text{C} \leq T \leq 500°\text{C} \\ -0.0006T + 0.493 & 500°\text{C} < T \leq 600°\text{C} \\ -3.15 \times 10^{-4}T + 0.316 & 600°\text{C} < T \leq 800°\text{C} \end{cases} \tag{4.10}$$

where ε'_v is the shear strain corresponding to the peak shear stress, f'_v is the peak shear stress in MPa, and γ_{vi} is the shear energy density in MPa, T is the temperature in °C, and the subscripts (1, 2, 3) denote the beam end section, beam center section, and column section, respectively. The optimum fitting of the simulated data is shown in Fig. 4.15 to 4.17.

Based on Fig. 4.15, it can be seen that the critical shear strain remains mainly

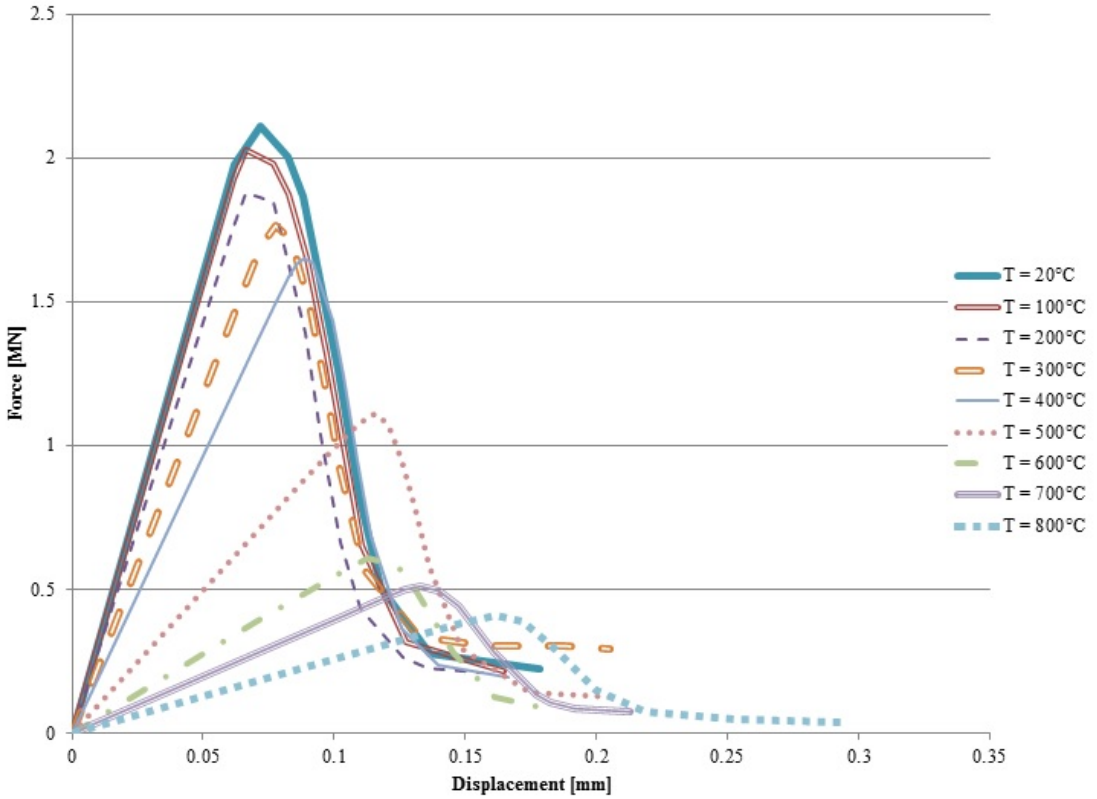

Figure 4.11: FE simulated force-displacement curve for tension of the column effective concrete section.

constant and then increases after 300°C. A single fit is chosen for the different potential damage zones due to the approximately similar behavior, taking into account the possible error range in the FE model results. Similar to the temperature-dependence of compressive strength, the shear strength monotonically decreases with temperature, as shown in Fig. 4.16. The energy dissipation shown in Fig. 4.17 also shows similar behavior to the compression energy, but with less difference in energy at room temperature. The differences can be due to the different transverse reinforcement ratios, with the largest ratio of transverse steel volume to concrete being in the beam end section, and the least in the column. When the temperature is beyond 500°C, the difference in energy dissipation gets diminished.

The temperature-dependent tension behavior of the effective section is likewise described. The finite element results can be found in Figs. 4.18 through 4.20, and the

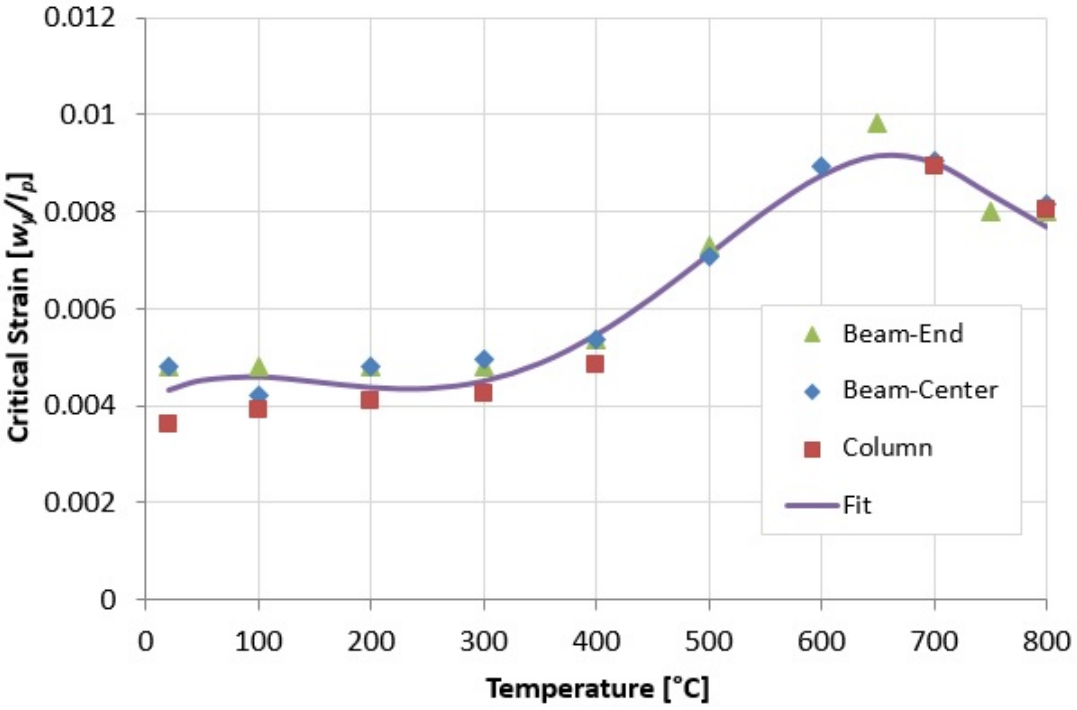

Figure 4.12: Simulated temperature-dependent critical strains at the peak compressive stress for different potential damage zones.

following empirical equations are proposed based on the optimum fits of the simulation results:

$$\varepsilon_t' = 1.40 \times 10^{-15}(T)^4 - 2.49 \times 10^{-12}(T)^3 + 2.04 \times 10^{-9}(T)^2 - 4.53 \times 10^{-7}(T) + 0.000265 \tag{4.11}$$

$$f_t' = \begin{cases} -0.0037(T) + 6.32 & 20°\text{C} \leq T \leq 400°\text{C} \\ 30 - 6.43 \times 10^{-8}(T)^3 - 1.445 \times 10^{-4}(T)^2 - 0.1104(T) & 400°\text{C} < T \leq 800°\text{C} \end{cases} \tag{4.12}$$

$$\gamma_{t1} = \begin{cases} 1.48 \times 10^{-6}(T)^2 - 0.00323(T) + 3.27 & 20°\text{C} \leq T \leq 400°\text{C} \\ 0.83 + 85.53e^{-0.0103(T)} & 400°\text{C} < T \leq 800°\text{C} \end{cases} \tag{4.13}$$

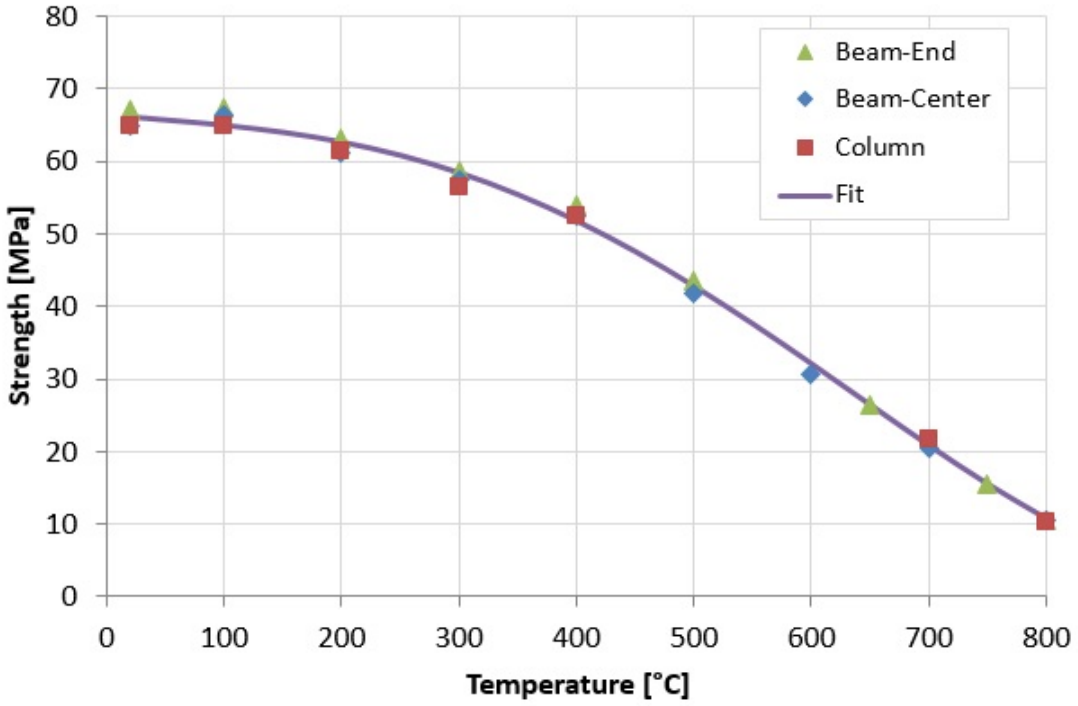

Figure 4.13: Simulated temperature-dependent compressive strengths for different potential damage zones.

$$\gamma_{t2} = \begin{cases} 7.28 \times 10^{-6}(T)^2 - 0.00562(T) + 3.3 & 20°\text{C} \leq T \leq 400°\text{C} \\ 0.832 + 85.53e^{-0.0103T} & 400°\text{C} < T \leq 800°\text{C} \end{cases} \tag{4.14}$$

$$\gamma_{t3} = \begin{cases} -0.00081(T) + 1.35 & 20°\text{C} \leq T \leq 400°\text{C} \\ 0.224 + 3.97e^{-0.004T} & 400°\text{C} < T \leq 800°\text{C} \end{cases} \tag{4.15}$$

where ε_t' is the tension strain corresponding to the peak stress in tension, f_t' is the peak tensile stress in MPa, γ_{ti} is the fracture energy density in kPa, T is in °C, and the subscripts (1, 2, 3) denote the beam end section, beam center section, and column section, respectively. Fig. 4.18 shows that the trend of the critical tensile strain appears far more regular than in compression or shear. For the temperature dependence of the tensile strength, Fig. 4.19 shows the peak tensile stress decreases with temperature,

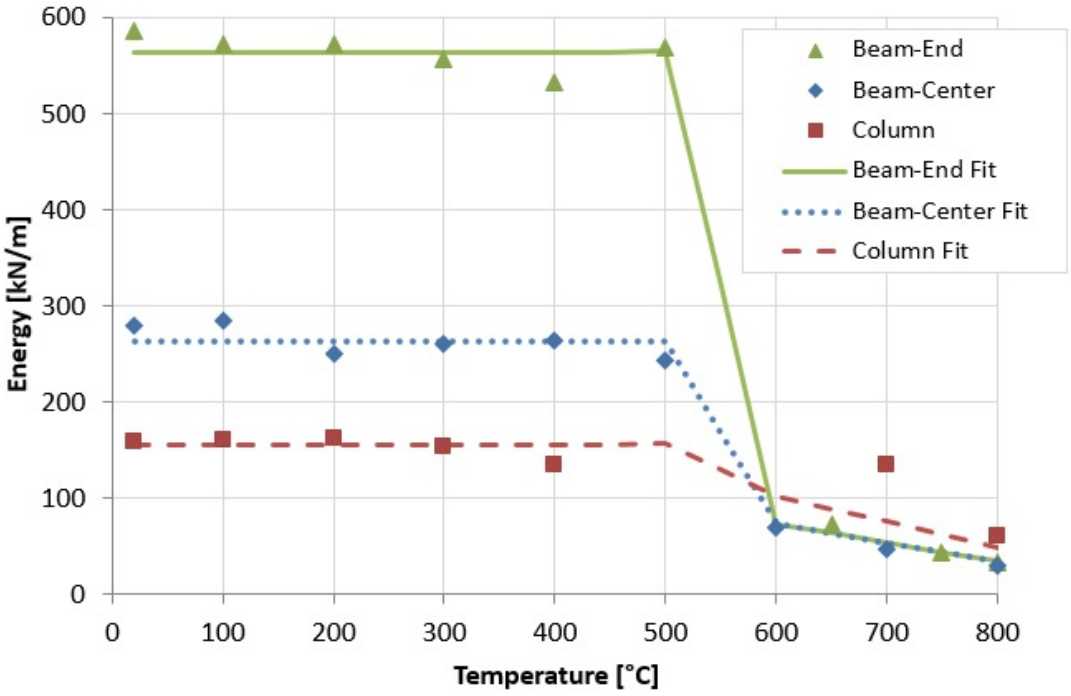

Figure 4.14: Simulated temperature-dependent fracture energies in compression for different potential damage zones.

with two apparent regimes, which is similar to the temperature dependence of material tensile strength that is used for the FE simulations. Fig. 4.20 shows the fracture energy decreases with temperature, for each potential damage zone. Unlike in compression and shear, the transverse reinforcement makes little difference in the tensile behavior of the concrete and therefore the difference in fracture energies among these three potential damage zones is smaller than that under compression and shear.

4.2.1 Calibration of thermo-dependent cohesive properties for longitudinal steel reinforcement

The longitudinal steel constitutive behavior does not require FE simulation since the bond-slip relation is assumed to be temperature independent. However, the tabulated data on temperature dependence of steel properties cannot directly be used in numerical implementation of the cohesive model. Therefore, piece-wise polynomial functions are

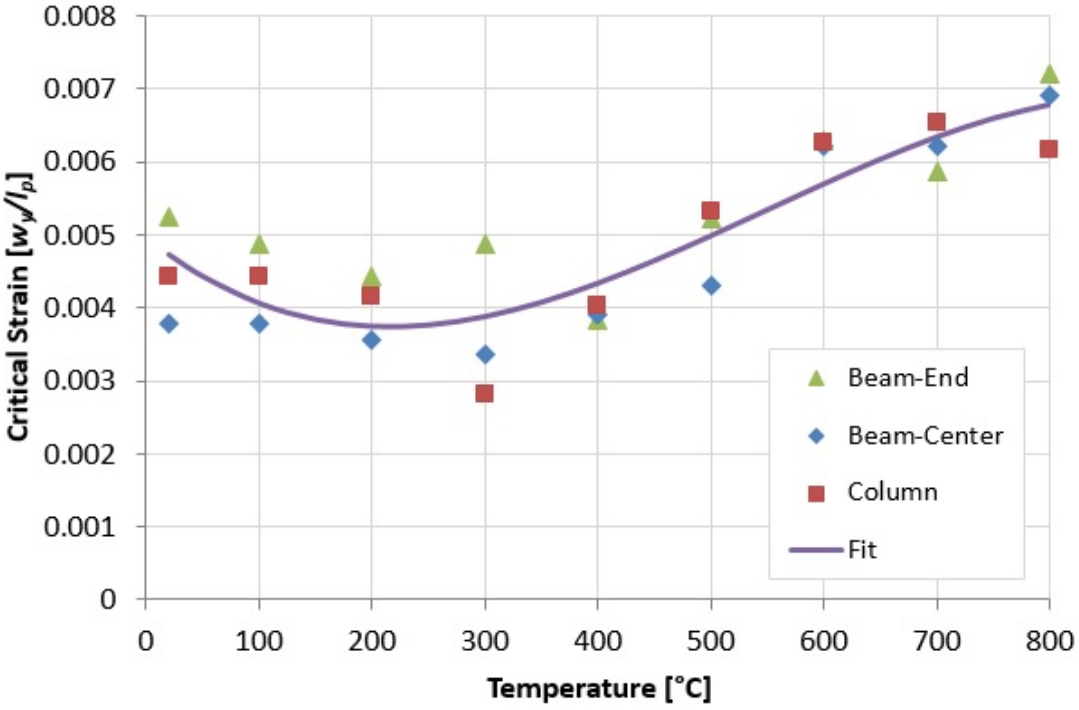

Figure 4.15: Simulated temperature-dependent critical strains at the peak shear stress for different potential damage zones.

proposed to fit the Eurocode 2 tabulated values (Table 3.1), as shown below:

$$\frac{f_u(T)}{f_u} = min \begin{cases} 1 \\ 5.107 - 0.0144T + (1.369 \times 10^{-5})T^2 + (4.369 \times 10^{-9})T^3 \end{cases} \tag{4.16}$$

$$\frac{f_y(T)}{f_y} = \begin{cases} 1 & T \leq 100°\text{C} \\ 1.195 - 0.00194T & 100°\text{C} < T \leq 400°\text{C} \\ 0.63525 - 0.0005406T & 400°\text{C} < T \leq 500°\text{C} \\ 5.397 - 0.0217T + (3.3 \times 10^{-5})T^2 & \\ \quad -(2.225 \times 10^{-8})T^3 + (5.587 \times 10^{-12})T^4 & T > 500°\text{C} \end{cases} \tag{4.17}$$

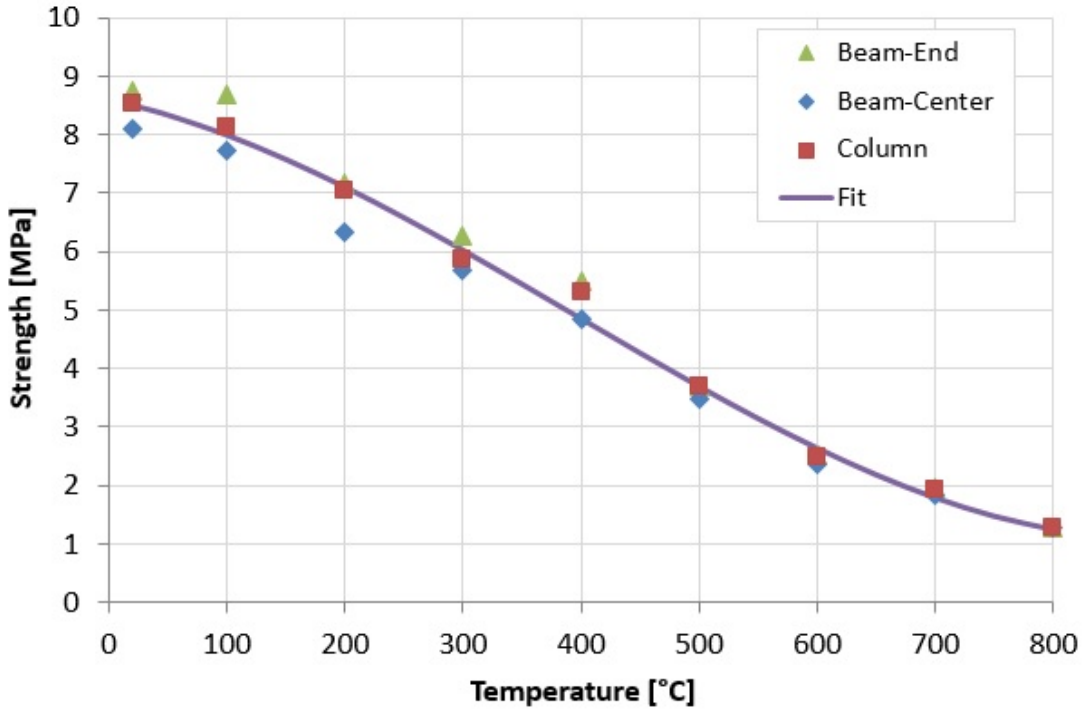

Figure 4.16: Simulated temperature-dependent shear strengths for different potential damage zones.

$$\frac{E_s(T)}{E_s} = \begin{cases} 1 & T \leq 100°\text{C} \\ 1.1 - 0.001(T) & 100°\text{C} < T \leq 501°\text{C} \\ 8.261 - 0.03257(T) + (4.865 \times 10^{-5})T^2 & \\ \qquad -(3.225 \times 10^{-8})T^3 + (7.955 \times 10^{-12})T^4 & T > 501°\text{C} \end{cases} \tag{4.18}$$

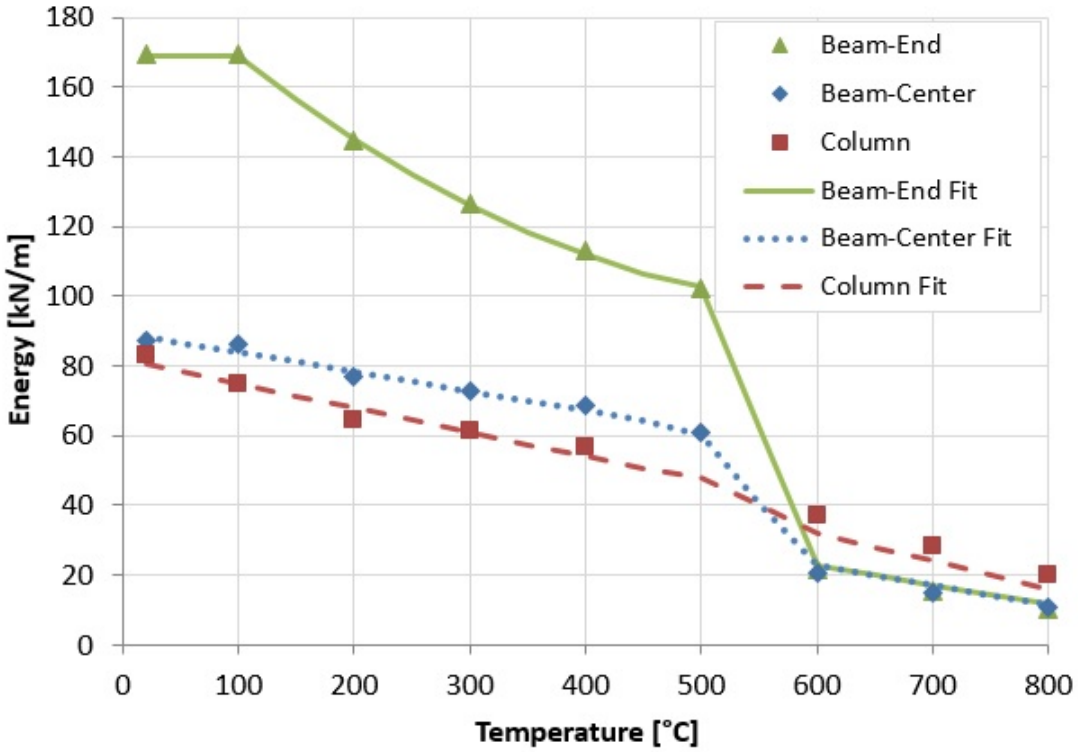

Figure 4.17: Simulated temperature-dependent shear fracture energies for different potential damage zones.

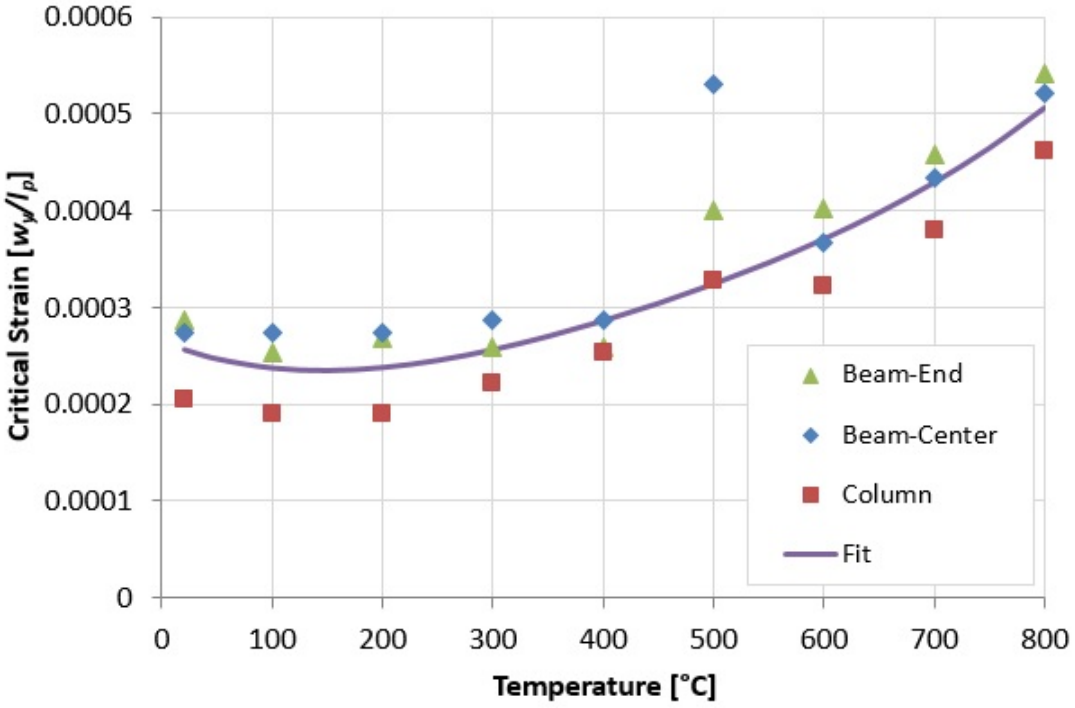

Figure 4.18: Simulated temperature-dependent critical strains at the peak tensile stress for different potential damage zones.

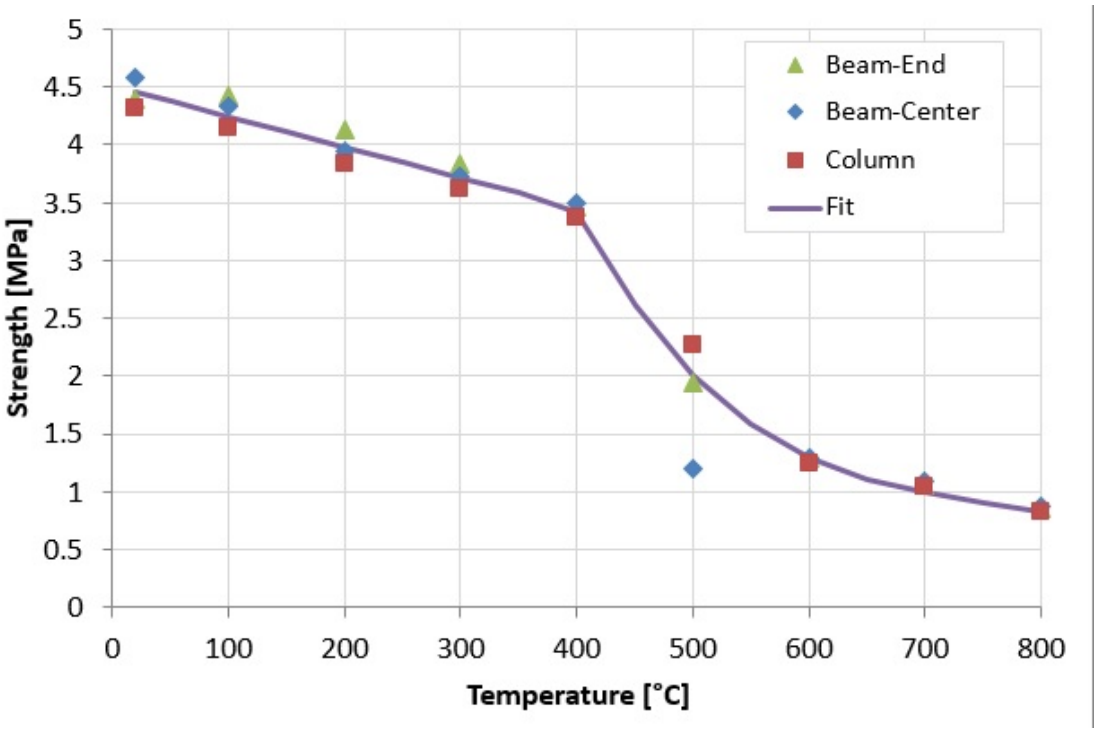

Figure 4.19: Simulated temperature-dependent tension strengths for different potential damage zones.

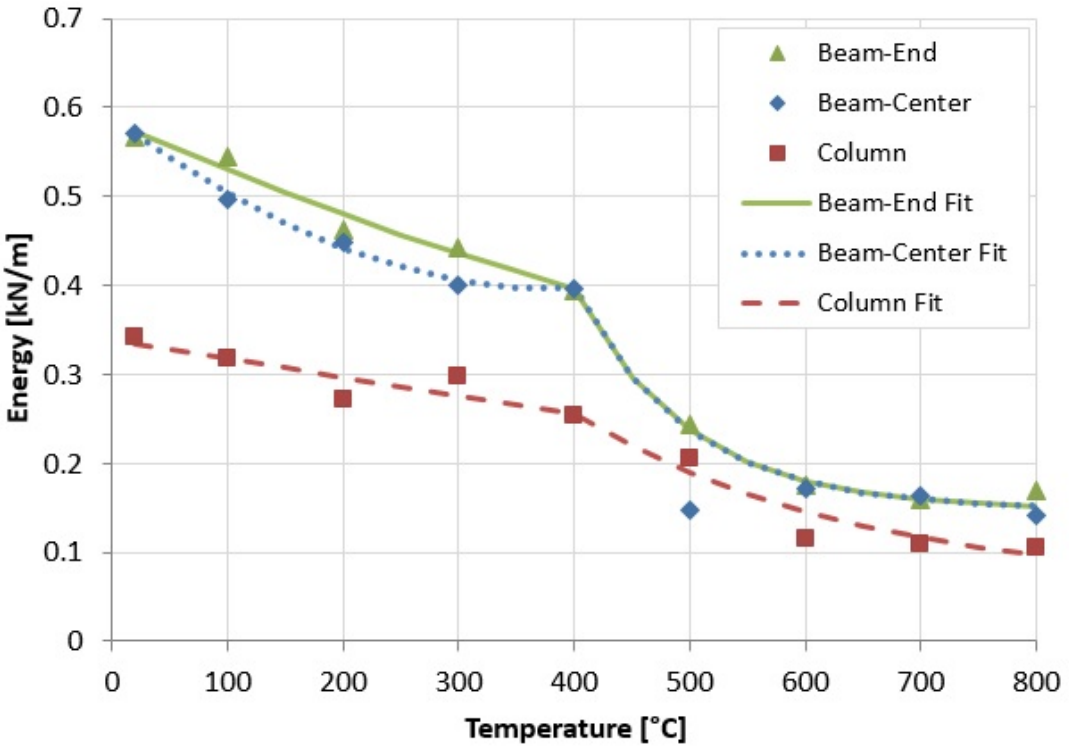

Figure 4.20: Simulate temperature-dependent tensile fracture energies for different potential damage zones.

Chapter 5

Simulations of Thermomechanical Response of Frame Subassemblage

The proposed two-scale model is now used to simulate the structural response of a RC frame subassemblage under thermomechanical loading. The loading scenarios include 1) mechanical loading at room temperature, 2) mechanical loading after 3-hour fire, and 3) mechanical loading after 6-hour fire. In parallel with the present model, conventional FE model is also adopted to simulate the response under these loading cases. It is shown that the structural response predicted by the proposed model agrees well with that predicted by the FE model. This confirms the validity of some key assumptions used in the two-scale model, which include the simplified constitutive law for cohesive element, FE-based calibration procedure, and the simplified temperature averaging procedure.

5.1 Description of Simulation Procedure

The structural dimension and design of the RC frame subassemblage considered in the study is shown in Fig. 4.1. Here we are interested in structural response of this frame subassemblage under three loading scenarios: 1) a displacement is applied at the center of the frame at the room temperature till the structural failure occurs, 2) the bottom

surface of the frame is subjected to fire for 3 hours and a centered displacement is then applied till the frame fails (Fig. 5.1), and 3) the bottom surface of the frame is subjected to fire for 6 hours and a centered displacement is then applied till the frame fails. Loading scenario 1) has often been used to investigate the frame response subjected to column removal [43] and loading scenarios 2) and 3) represents the frame response subjected to column removal in a fire environment. In the present simulation, the Eurocode standard fire curve is used to obtain the time evolution of the temperature on the bottom surface of the frame.

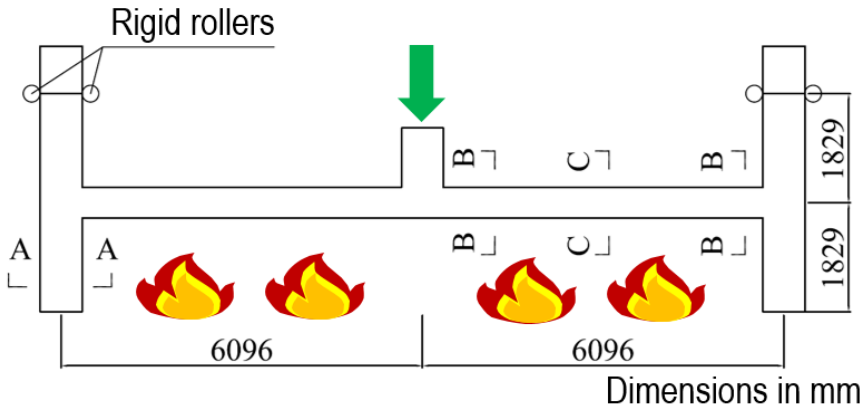

Figure 5.1: Thermomechanical loading on frame subassemblage.

For loading scenarios 2) and 3), the displacement is applied in a very short period of time compared to duration of the previous fire loading. Therefore, we may freeze the temperature field of the frame subassemblage when applying the displacement. This allows us to decouple the thermal and mechanical analyses, even though the mechanical analysis needs the temperature field from the fire loading to determine the structural response at elevated temperatures. In this study, the thermal analysis is performed by using the standard FE procedure, where we use the following thermal properties of concrete from the Eurocode 2 [47], i.e. the thermal conductivity $k_c = 2 - 0.002451 \times$

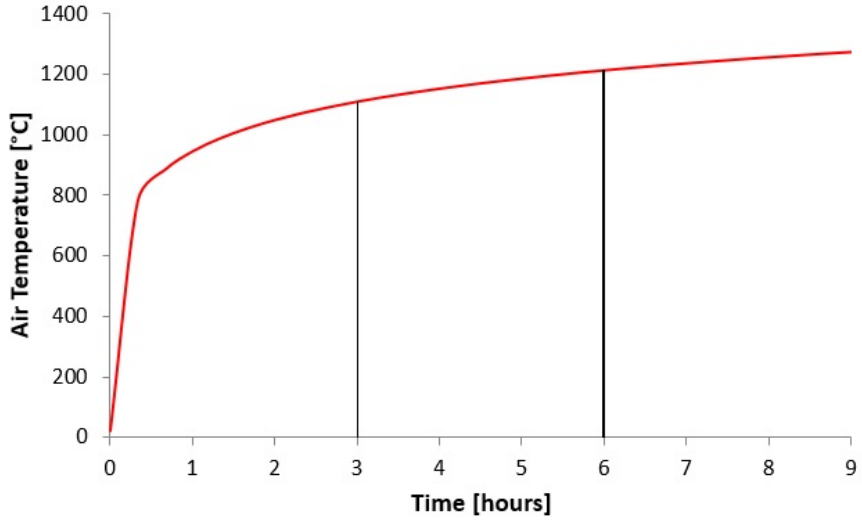

Figure 5.2: Standard fire curve from Eurocode 2 [47].

$T + 1.07 \times 10^{-6} \times T^2$ [W/mK] and heat capacity of concrete [J/kg K] is

$$C = \begin{cases} 900 & 20°\text{C} \leq T \leq 100°\text{C} \\ 800 + T & 100°\text{C} < T \leq 200°\text{C} \\ 1000 + \frac{1}{2}(T - 200) & 200°\text{C} < T \leq 400°\text{C} \\ 1100 & 400°\text{C} < T \leq 1200°\text{C} \end{cases} \tag{5.1}$$

Note that the thermal properties of steel reinforcement are not included here because the relative small amount of reinforcement would not significantly alter the heat diffusion in the concrete. Fig. 5.3 shows the temperature distribution in the cross section of the beam after 3 hour and 6 hour of fire loading. Since we consider a uniform fire across the beam span, it is clear that the temperature distribution shown in Fig. 5.3 is invariant along the beam span.

Subsequent to the thermal analysis, mechanical analysis is performed to investigate the response of the frame subassemblage subjected to displacement-controlled loading applied at the center of the frame. Two numerical models are used here: 1) the proposed two-scale model, and 2) conventional FE model. Fig. 5.4 show the representations of the frame subassemblage using these two models. For the two-scale model, the constitutive relationship of the cohesive elements, which represent the potential damage

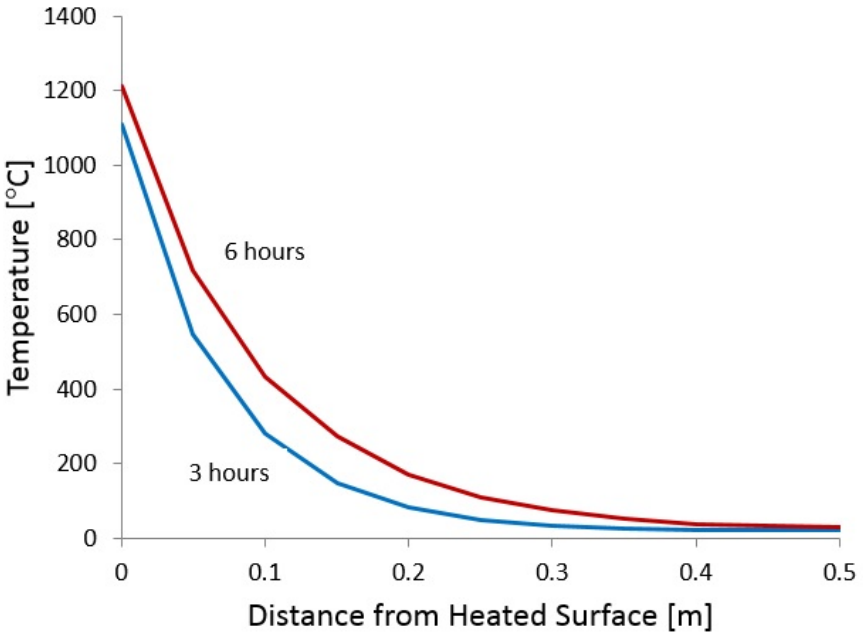

Figure 5.3: Temperature distributions through beam cross-section at 3 hours and 6 hours on the standard fire curve.

zones, has been calibrated based on the fine-scale FE analysis as presented in Chapter 4. Furthermore, according to Eqs. 2.1 and 2.2, the cohesive model also needs the input of the thermal expansion coefficients of concrete and steel α_c and α_s . Here we assume that α_c is approximately equal to α_s, and their temperature dependence follows an empirical equation [47]:

$$\alpha_c = \begin{cases} \dfrac{\left(2.3\times10^{-11}\right)T^3 + \left(9.0\times10^{-6}\right)T - 1.8\times10^{-4}}{T - 20°\text{C}} & 20°\text{C} < T \le 700°\text{C} \\ \dfrac{0.014}{T - 20°\text{C}} & 700°\text{C} < T \le 1200°\text{C} \end{cases} \tag{5.2}$$

Based on the temperature field calculated from the aforementioned thermal analysis, the temperature input for each Gauss point of the cohesive elements is obtained based on the averaging procedure described in Chapter 2 (Section 2.2.2). With the calibrated thermo-dependent cohesive properties (Chapter 4), the cohesive element model is used to simulate the response of the frame subassemblage under the mechanical loading. For the present simulations, the cohesive element model is implemented in the commercial FE software ABAQUS/Explicit, where a material subroutine is coded for the cohesive

element.

For the FE simulations, the constitutive relationship of concrete material is described by the damage-plasticity model [51]and the steel behavior is described by the standard kinematic hardening model. The temperature dependent material properties for concrete and steel follow Table 4.1, Table 3.1, and Eqs. 3.1-3.6. Eq. 5.2 is used for the thermal expansion coefficient of concrete and steel. Similar to the fine-scale FE-based calibration presented in Chapter 4, the mesh size of the finite elements for concrete material is set to be 50 mm, which is equal to the crack band width, and the steel reinforcement is modeled as the steel trusses. The temperature field obtained by the thermal analysis is directly input to the Gauss point of each element, and therefore the constitutive behavior of each Gauss point is different due to the non-uniform temperature field. Due to the geometry symmetry, only half of the frame subassemblage is simulated by the FE model to save computational time. Similar to the aforementioned cohesive element modeling, the FE simulation is performed using ABAQUS/Explicit.

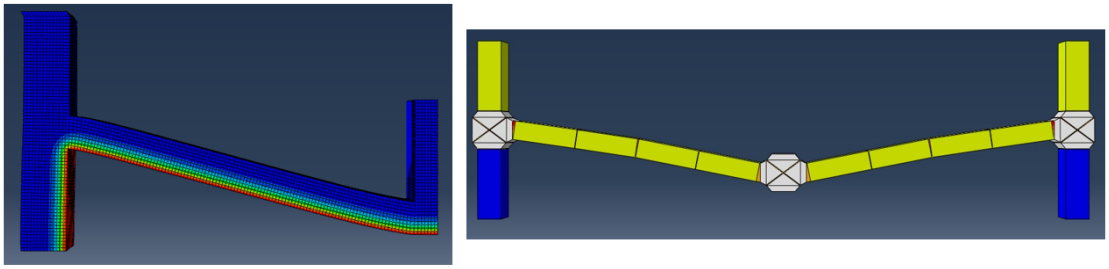

a) b)

Figure 5.4: Numerical simulation of frame subassemblage under mechanical loading: a) two-scale model, and b) FE model.

5.2 Results and Discussion

Figs. 5.5, 5.6, and 5.7 present the simulated load-displacement response of the frame subassemblage under the three loading scenarios. It can be seen that the load-displacement curves exhibit a similar qualitative behavior for all three loading scenarios: after the initial elastic response, it reaches a peak load followed by a pronounced softening branch, and subsequently the load capacity increases again with the applied displacement till

a final sudden drop in load capacity. The physical mechanism that could explain such a complex behavior can be described as follows: the subassemablge first undergoes a linear elastic deformation, and some level of tensile damage is developed at the bottom of the beam at the center of the subassemablage. Upon further loading, concrete at the top part of the beam at the center of the subassemablage starts to experience compressive damage, which lead to some nonlinear pre-peak response of the load-displacement curve. Once the significant amount of compressive damage is developed, the subassembalge reaches its peak strength, and subsequently exhibits a softening response. With the significant increase in displacement, the catenary action is eventually developed, where the entire beam is under tension giving rise to the second ascending branch of the load-deflection curve. Finally, the steel reinforcement ruptures, and the entire subassemblage falls apart, which is signified by the final sudden drop in load capacity.

By comparing the load-deflection curves among these three loading scenarios, it is seen that the first peak load does not vary much. This is because the first peak load is due to the compressive damage of concrete at the top part of the beam near the center of the subassemblage. Due to the low thermal conductivity of concrete, the temperature at top part of the beam is almost the same for all three loading scenarios, and therefore the first peak load is not affected much by the fire loading. By contrast, the load capacity at the final failure point differs quite a bit among these loading scenarios simply because the final failure is caused by the steel rupture, which is strongly dependent on the temperature field.

Figs. 5.8 and 5.9 show the simulated damage extent of concrete at the first peak load point predicted by the proposed model and FE model for loading scenarios 2 and 3. It can be seen that the predictions by these two models are pretty consistent. The key difference is that in the FE model the damage is more distributed whereas in the proposed model the damage can only occur in the cohesive element. Nevertheless, it should be emphasized here that the cohesive element here represents a finite-size potential damage zone, which could exhibit a diffused damage pattern. Figs. 5.10 and 5.11 show the simulated plastic strains in steel reinforcement at the final failure points. Again, it can be seen that both models predict a similar response. Therefore, we may conclude that the proposed two-scale model is able to qualitatively capture the complex nonlinear behavior of the RC frame structures at elevated temperatures.

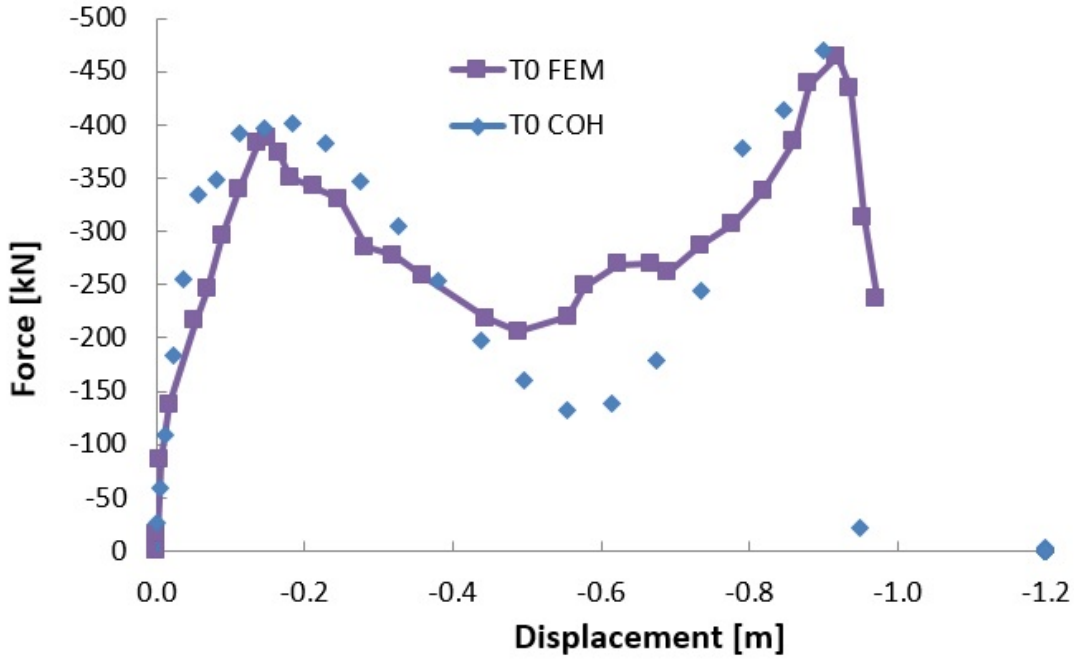

Figure 5.5: Load-displacement curve for loading scenario 1.

Now we compare quantitatively the simulated load-deflection curves by the present model and the FE model. It can be seen that for all loading scenarios the predictions of the initial ascending branch, the first peak load, and the softening branch are consistent between these two models, and the FE model shows the longitudinal steel picking up load sooner than in the cohesive element model in each of the models. The difference in the second ascending branch between these two models get more pronounced for the case of elevated temperatures (loading scenarios 2 and 3). This could be due to the temperature averaging procedure that we used, where we simply average the temperature in the cross section. A more realistic approach should obtain the equivalent temperature for the Gauss point such that the mechanical behavior of the Gauss point is equivalent to the net behavior of the concrete cross section with the non-uniform temperature. Since the temperature dependence of concrete properties is nonlinear, and therefore the resulting equivalent temperature for the Gauss point would not be equal to the simple average of the temperature field. Nevertheless, we observe that for all loading scenarios the predicted total energy dissipations (i.e. the area under the load-deflection curve) by

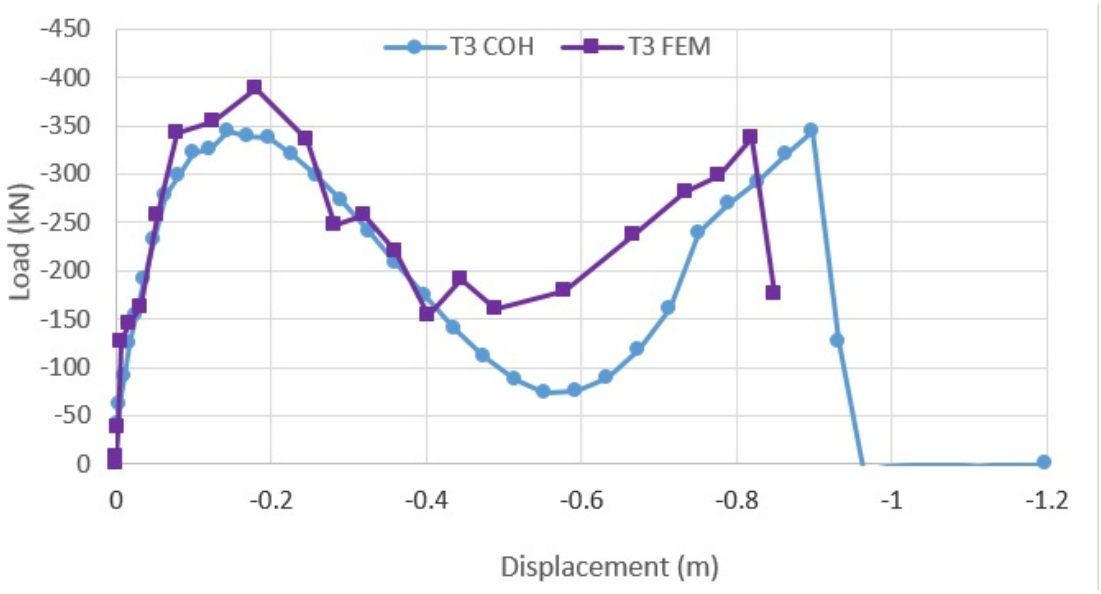

Figure 5.6: Load-displacement curve for loading scenario 2.

these two models are almost the same, which is critical for predicting the global collapse behavior of RC structures.

5.3 Future Extension to Simulations of Fire-Induced Building Collapse

It is worthwhile to comment on the future extension of the proposed two-scale model for simulation of fire-induced collapse of large-scale RC frames. Based on the aforementioned numerical simulations of the frame subassemblage, we can conclude that the proposed model is able to reasonably well capture the nonlinear structural behavior of the frame, especially in terms of the first peak load and the total energy dissipation capacity. This shows the promise to use this model for simulations of the fire-induced collapse of large-scale RC frames because for large-scale structures, the detailed time history of collapse of individual structural component is not significant as long as the model can capture the total collapse time of each structural component, which is dictated by the total energy dissipation capacity (the detailed shape of the load-deflection curve is not important). Furthermore, previous study [27] has successfully applied the

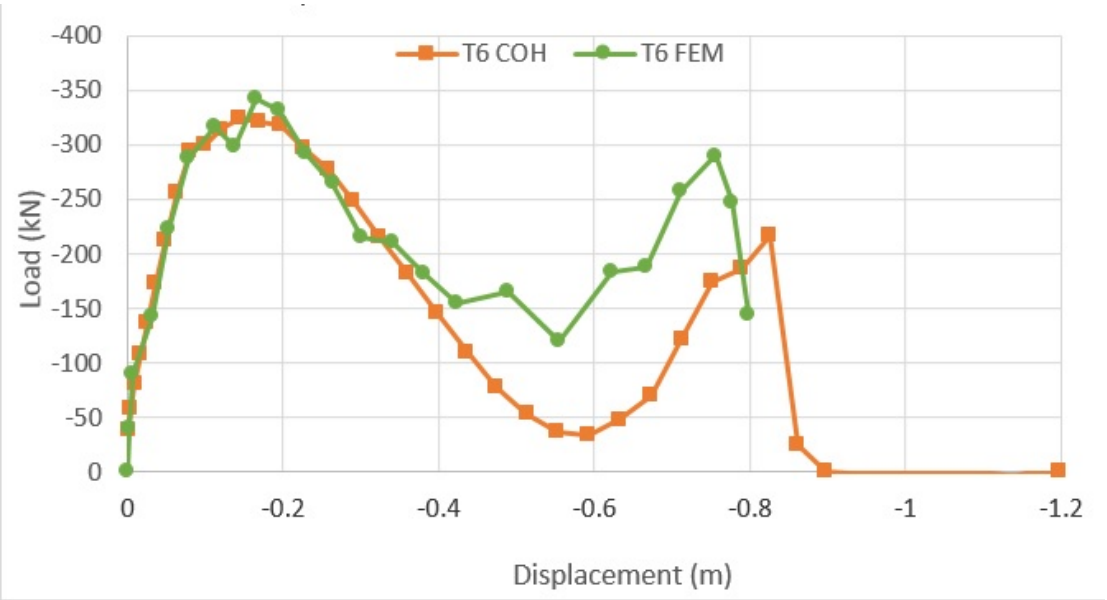

Figure 5.7: Load-displacement curve for loading scenario 3.

cohesive element model for progressive collapse of RC frame structures, where the cohesive elements can be deleted once they lose the load capacity and impact between the elastic elements can be handled by a set of contact laws. Therefore, we foresee that the proposed two-scale model could provide us an effective means to investigate the post-fire structural integrity and potential collapse patterns of large-scale RC frame structures.

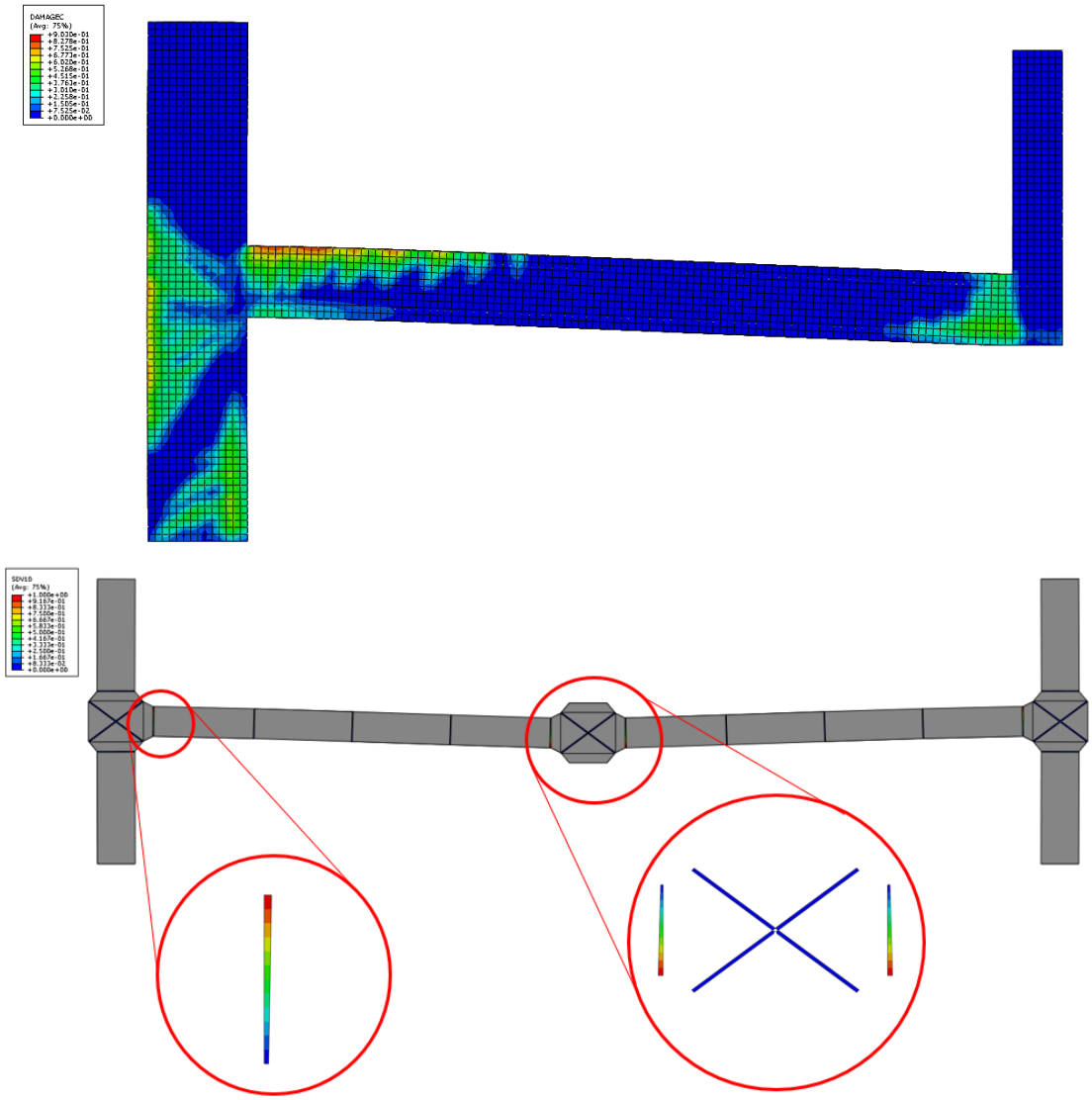

Figure 5.8: Predicted concrete damage at the first peak load (3 hours fire loading): a) FE model, and b) cohesive model.

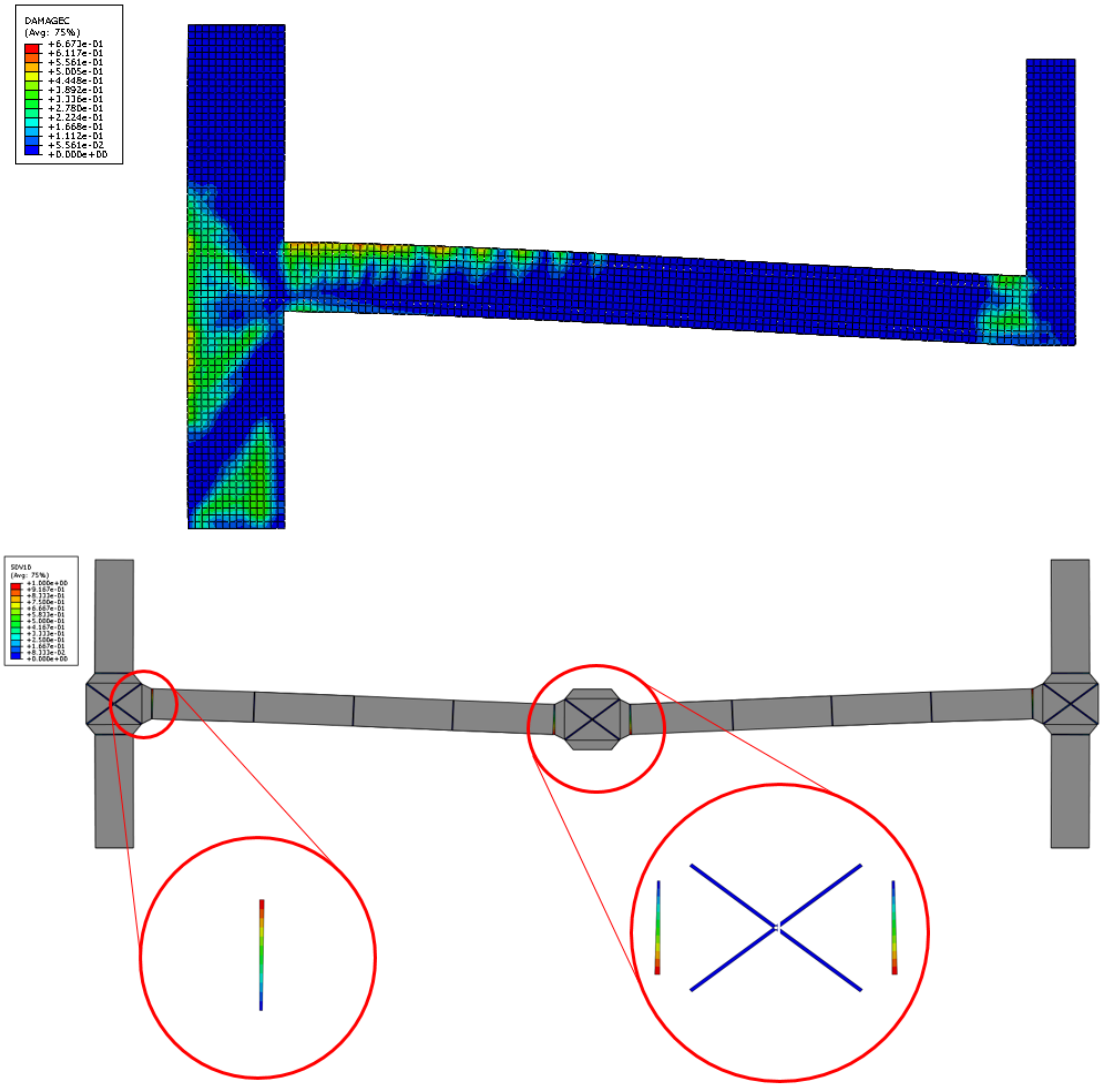

Figure 5.9: Predicted concrete damage at the first peak load (6 hours fire loading): a) FE model, and b) cohesive model.

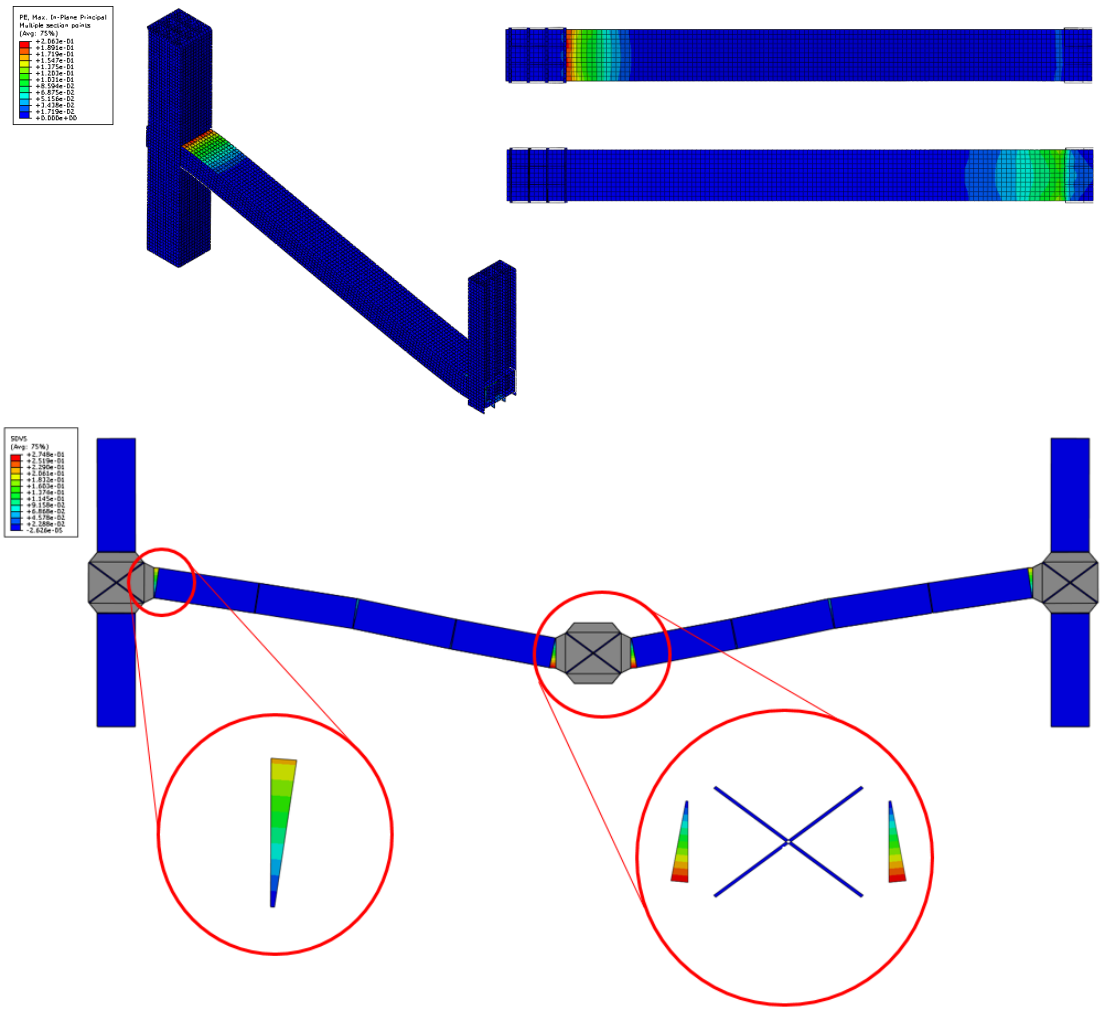

Figure 5.10: Predicted logarithmic strain in steel at ultimate failure (3 hours fire loading): a) FE model, and b) cohesive model.

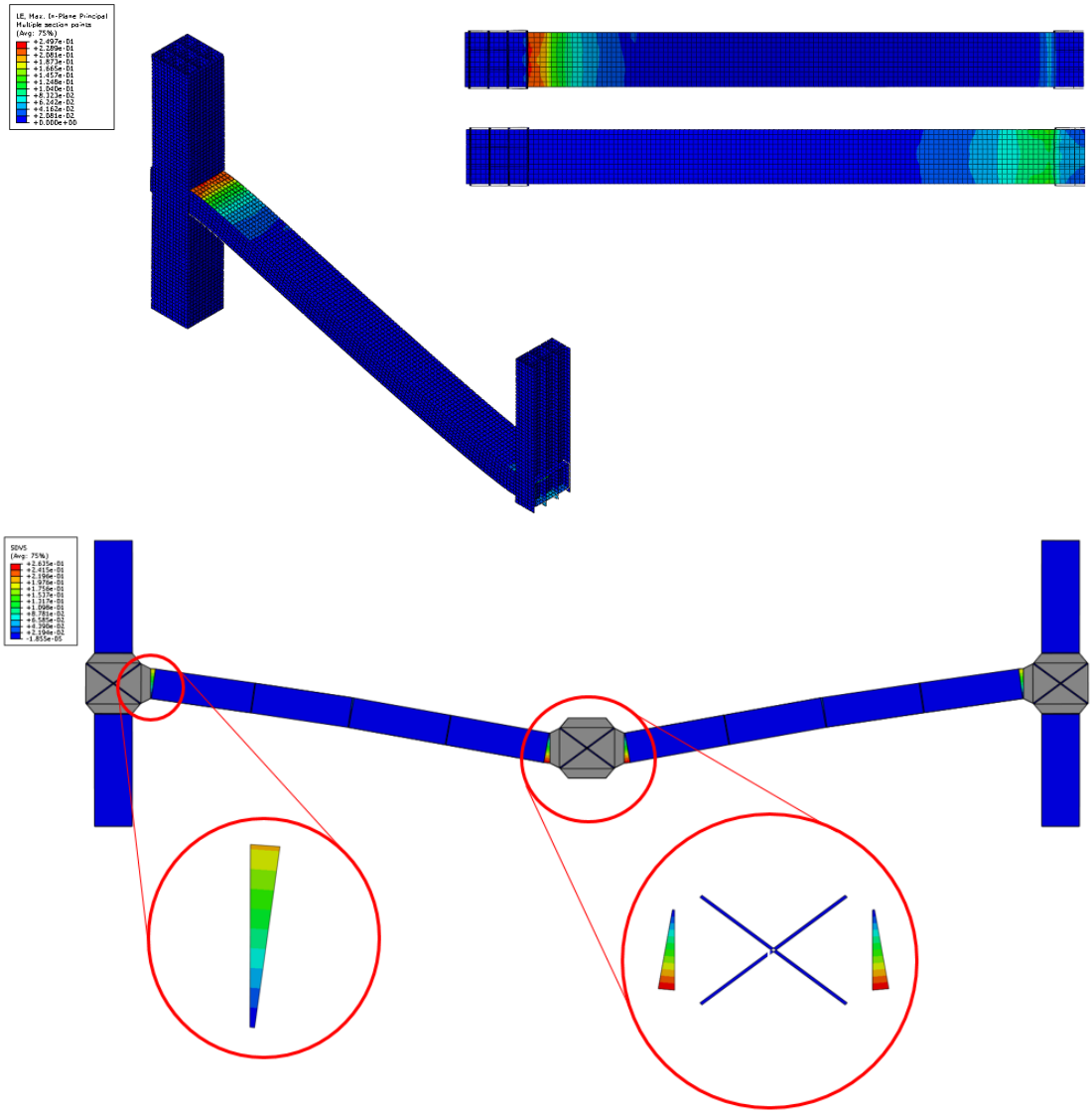

Figure 5.11: Predicted logarithmic strain in steel at ultimate failure (6 hours fire loading): a) FE model, and b) cohesive model.

Chapter 6

Conclusion

This study develops a two-scale thermomechanical model which can efficiently simulate the behavior of RC frame structures under thermomechanical loading.

- The proposed cohesive model can effectively account for fracture and damage of RC structural components under general mixed-mode loading. With the fine-scale FE-based calibration of the cohesive properties, the behavior of global structural components is directly related to the constitutive behavior of materials, where the effects of temperature and structural size and geometry on the structural behavior can be well captured. Therefore, the proposed model can be calibrated by using the material tests of concrete and steel at high temperatures, as demonstrated in the present study.

- The cohesive model can capture failure mechanisms of structural elements observed in tests, and gives reasonable correspondence to finite element modeling with a much lower computational cost. The push-down test demonstrates the ability of the model to capture the mechanisms of concrete crushing and steel yielding, similar to the detailed FE simulation. The overall behavior of the cohesive model also reflects the peak load and energy dissipation of the structural system, which governs the collapse behavior of the structure.

- The proposed two-scale model can be used as an efficient method for exploring the structural resistance of RC frames against fire loading and predicting the

resulting structural behavior, including both structural damage as well as large-scale structural collapse. Therefore, we foresee that this model can be extended to general 3D RC buildings against thermomechanical loading.

Bibliography

[1] M. Karter. Fire loss in the united states during 2012. Technical report, National Fire Protection Agency, Quincy, MA, September 2013. Retrieved from http://www.nfpa.org/assets/files/PDF/OS.fireloss.pdf.

[2] J. Beitel and N. Iwankiw. Analysis of needs and existing capabilities for full-scale fire resistance testing. Technical Report 1, National Institute of Standards and Technology, October 2008. Retrieved from http://www.bfrl.nist.gov/866/pubs/NISTGCR02-843.pdf.

[3] Y. Alashker, H. Li, and S. El-Tawil. Approximations in progressive collapse modeling. *Journal of Structural Engineering, ASCE*, 137(9):914–924, 2011.

[4] E. Masoero, F. K. Wittel, H. J. Herrmann, and B. M. Chiaia. Progressive collapse mechanisms of brittle and ductile framed structures. *Journal of Engineering Mechanics, ASCE*, 136(8):987–995, 2010.

[5] G. Kaewkulchai and E.B. Williamson. Beam element formulation and solution procedure for dynamic progressive collapse analysis. *Computers & Structures*, 82(7):639–651, 2004.

[6] DE Grierson, L. Xu, and Y. Liu. Progressive-failure analysis of buildings subjected to abnormal loading. *Computer-Aided Civil and Infrastructure Engineering*, 20(3):155–171, 2005.

[7] K. Khandelwal and S. El-Tawil. Pushdown resistance as a measure of robustness in progressive collapse analysis. *Engineering Structures*, 33(9):2653–2661, 2011.

[8] Y. Bao, S. K. Kunnath, S. El-Tawil, and H. S. Lew. Macromodel-based simulation of progressive collapse: Rc frame structures. *Journal of Structural Engineering, ASCE*, 134(7):1079–1091, 2008.

[9] Y. Anderberg and J. Thelanderssson. Stress and deformation characteristics of concrete at high temperatures. Technical report, Lund Institute of Technology, Lund, Sweden, 1976.

[10] K.-Y. Shin, S.-B. Kim, J.-H. Kim, M. Chung, and P.-S. Jung. Thermal-physical properties and transient heat transfer of concrete at elevated temperature. *Nuclear Engineering and Design*, 212:233–241, 2002.

[11] Z. P. Bažant and M. F. Kaplan. *Concrete at High Temperatures: Material Properties and Mathematical Models*. Longman, 1996.

[12] G. Khoury, P. Sullivan, and B. Grainger. Transient thermal strain of concrete: Literature review, conditions with specimen, and individual constitutive behavior. *Magazine of Concrete Research*, 37(132):131–144, 2005.

[13] K. Willam, I. Rhee, and Y. Xi. Thermal degradation of heterogeneous concrete materials. *Journal of Materials in Civil Engineering*, 17(3):276–286, 2005.

[14] B. F. Ulm, O. Coussy, and Z.P. Bažant. The chunnel fire. i: Chemoplastic softening in rapidly heated concrete. *Journal of Engineering Mechanics*, 125(3):272–282, 1999.

[15] Z. P. Bažant and J. Chern. Stress-induced thermal and shrinkage strains in concrete. *Journal of Engineering Mechanics*, 113(10):1493–1511, 1987.

[16] G. Di Luzio and G. Cusatis. Hygro-thermo-chemical modeling of high performance concrete. i: Theory. *Cement and Concrete Composites*, 31:301–308, 2009.

[17] K. Willam, I. Rhee, and B. Shing. Interface damage model for thermomechanical degradation of heterogeneous materials. *Computer Methods in Applied Mechanics and Engineering*, 193(30–32):3327–3350, 2004.

[18] P. Grassl and C. Pearce. Mesoscale approach to modeling concrete subjected to thermomechanical loading. *Journal of Engineering Mechanics, ASCE*, 136(3):322–328, 2010.

[19] B. F. Ulm, P. Acker, and M. Lvy. The chunnel fire. II: Analysis of concrete damage. *Journal of Engineering Mechanics*, pages 283–289, March 1999.

[20] I. Fletcher, A. Borg, N. Hitchen, and S. Welch. Performance of concrete in fire: A review of the state of the art, with a case study of the windsor tower fire. In P. V. Real, J.-M. Franssen, and N. Lopes, editors, *Proceedings of the 4th International Workshop in Structures in Fire*, pages 779–790, Aveiro, Portugal, 2006.

[21] S. F. El-Fitiany and M. A. Youssef. Assessing the flexural and axial behaviour of reinforced concrete members at elevated temperatures using sectional analysis. *Fire Safety Journal*, 44(5):691–703, 2009.

[22] L. Gosselin, A. Bejan, and S. Lorente. Combined 'heat flow and strength optimization of geometry: mechanical structures most resistant to thermal attack. *International Journal of Heat and Mass Transfer*, 47(14–16):3477–3489, 2004.

[23] Z. Huang. The behaviour of reinforced concrete slabs in fire. *Fire Safety Journal*, 45(5):271–282, 2010.

[24] A. Vaziri, A. Ajdari, H. Ali, and A.A. Twohig. Structural analysis of reinforced concrete chimneys subjected to uncontrolled fire. *Engineering Structures*, 33(10):2888–2898, 2011.

[25] P. Pfeiffer, J. Kennedy, and A. Marchertas. Thermal effects in the overpressurization response of reinforced concrete containment. *Nuclear Engineering and Design*, 120:25–34, 1990.

[26] N. Yamazaki, M. Yamazaki, T. Mochida, A. Mutoh, T. Miyashita, M. Ueda, T. Hasegawa, K. Sugiyama, K. Hirakawa, R. Kikuchi, M. Hiramoto, and K. Saito. Structural behavior of reinforced concrete structures at high temperatures. *Nuclear Engineering and Design*, 156, 1995.

[27] Jia-Liang Le and Bing Xue. Probabilistic analysis of reinforced concrete frame structures against progressive collapse. *Engineering Structures*, 76:313–323, October 2014.

[28] G. I. Barrenblatt. The mathematical theory of equilibrium of cracks in brittle fracture. *Advances in Applied Mechanics*, 7:55–129, 1959.

[29] D. S. Dugdale. Yielding of steel sheets continuity slits. *Journal of Mechanics and Physics of Solids*, 8:100–104, 1960.

[30] A. Hillerborg, M. Modeer, and P. E. Petersson. Analysis of crack formation and crack growth in concrete by means of fracture mechanics and finite elements. *Cement and Concrete Research*, 6(6):773–782, 1976.

[31] Z. P. Bažant and J. Planas. *Fracture and Size Effect in Concrete and Other Quasibrittle Materials*. 1998.

[32] F.R. Shanley. Inelastic column theory. *Journal of the Aeronautical Sciences (Institute of the Aeronautical Sciences)*, 14(5):261–268, 1947.

[33] Z.P. Bažant and L. Cedolin. *Stability of structures: elastic, inelastic, fracture and damage theories*. Oxford University Press, New York, 1991.

[34] L.N. Lowes and A. Altoontash. Modeling reinforced-concrete beam-column joints subjected to cyclic loading. *Journal of Structural Engineering*, 129(12):1686–1697, 2003.

[35] H. Shiohara. Reinforced concrete beam-column joints: An overlooked failure mechanism. *ACI Structural Journal*, 109(1):65–74, 2012.

[36] G. Cusatis, Z.P. Bažant, and L. Cedolin. Confinement-shear lattice model for concrete damage in tension and compression: I. theory. *Journal of Engineering Mechanics*, 129(12):1439–1448, 2003.

[37] GT Camacho and M. Ortiz. Computational modelling of impact damage in brittle materials. *International Journal of Solids and Structures*, 33(20):2899–2938, 1996.

[38] Z.P. Bažant and M. Verdure. Mechanics of progressive collapse: Learning from world trade center and building demolitions. *Journal of Engineering Mechanics*, 133(3):308–319, 2007.

[39] Z.P. Bažant, J.L. Le, F.R. Greening, and D.B. Benson. What did and did not cause collapse of World Trade Center twin towers in New York? *Journal of Engineering Mechanics*, 134(10):892–906, 2008.

[40] B.A. Izzuddin, A.G. Vlassis, A.Y. Elghazouli, and D.A. Nethercot. Progressive collapse of multi-storey buildings due to sudden column loss–Part I: Simplified assessment framework. *Engineering Structures*, 30(5):1308–1318, 2008.

[41] K.A. Seffen. Progressive collapse of the world trade center: simple analysis. *Journal of Engineering Mechanics*, 134(2):125–132, 2008.

[42] G. Xu and B.R. Ellingwood. Probabilistic robustness assessment of pre-northridge steel moment resisting frames. *Journal of Structural Engineering*, 137(9):925–934, 2011.

[43] H.S. Lew, Yihai Bao, Fahim H. Sadek, and Joseph A. Main. *An Experimental and Computational Study of Reinforced Concrete Assemblies under a Column Removal Scenario*. Number NIST TN - 1720. 2011.

[44] H. Sezen and J.P. Moehle. Bond-slip behavior of reinforced concrete members. In *Proceedings of Fib Symposium on Concrete Structures in Seismic Regions*, 2003.

[45] ACI Committee 408. *Bond and Development of Straight Reinforcing Bars in Tension (ACI 408R-03)*. American Concrete Institute, Detroit, Michigan, US, 2003.

[46] M. Jirásek and Z. P. Bažant. *Inelastic Analysis of Structures*. Wiley, 2002.

[47] EN 1992-1-2: Eurocode 2: Design of concrete structures – Part 1-2: General rules structural fire design, 2004.

[48] L.E. Aycardi, J.B. Mander, and A.M. Reinhorn. Seismic resistance of reinforced concrete frame structures designed only for gravity loads: Experimental performance of subassemblages. *ACI Structural Journal*, 91(5):552–563, 1994.

[49] G. Parra-Montesinos and J.K. Wight. Modeling shear behavior of hybrid RCS beam-column connections. *Journal of Structural Engineering*, 127(1):3–11, 2001.

[50] N. Mitra and L.N. Lowes. Evaluation, calibration, and verification of a reinforced concrete beam-column joint model. *Journal of Structural Engineering*, 133(1):105–120, 2007.

[51] J. Lee and G.L. Fenves. Plastic-damage model for cyclic loading of concrete structures. *Journal of Engineering Mechanics*, 124(8):892–900, 1998.

[52] J. Ding, G.-Q. Li, and Y. Sakumoto. Parametric studies on fire resistance of fire-resistant steel members. *Journal of Constructional Steel Research*, 60(7):1007–1027, 2004.

[53] J.M. Franssen, G.M.E. Cooke, and D.J. Latham. Numerical simulation of a full scale fire test on loaded steel framework. *Journal of Constructional Steel Research*, 35:377–408, 1995.

[54] Qianru Guo, Kaihang Shi, Zili Jia, and Ann E. Jeffers. Probabilistic evaluation of structural fire resistance. *Fire Technology*, 49(3):793–811, 2013.

[55] E. Unluoglu, I. B. Topcu, and B. Yalaman. Concrete cover effect on reinforced concrete bars exposed to high temperatures. *Construction and Building Materials*, 21(6):1155–1160, 2007.

[56] M.A. Youssef and M. Moftah. General stressstrain relationship for concrete at elevated temperatures. *Engineering Structures*, 29(10):2618–2634, 2007.

[57] J. Lee, Y. Xi, K. Willam, and Y. Jung. A multiscale model for modulus of elasticity of concrete at high temperatures. *Cement and Concrete Research*, 39(9):754–762, 2009.

[58] A. Menou, G. Mounajed, H. Boussa, C. L. Borderie, and K. Lafdi. Thermal damage approach of concrete: Application to specimens subjected to combined compressive and high temperature loads. *High Temperature Materials and Processes*, 27(1):23–40, 2007.

[59] W. Nechnech, F. Meftah, and J. M. Reynouard. An elasto-plastic damage model for plain concrete subjected to high temperatures. *Engineering Structures*, 24(5):597–611, 2002.

[60] J. Lee, Y. Xi, and K. Willam. Properties of concrete after high-temperature heating and cooling. *ACI Materials Journal*, 105(4):334–341, 2008.

[61] P.J.E. Sullivan and R. Sharshar. The performance of concrete at elevated temperatures (as measured by the reduction in compressive strength. *Fire Technology*, August 1992.

[62] J.A. Purkiss and J.W. Dougill. Apparatus for compression tests on concrete at high temperatures. *Magazine of Concrete Research*, (83), 1973.

[63] U. Schneider. Properties of material at high temperatures-concrete. Technical report, RILEM-Committee 44-PHT, Department of Civil Engineering, University of Kassel, 1985.

[64] F. Furamura, C. H. Oh, T. Ave, and W. J. Kim. Simple formulation for stress-strain relationship of normal concrete at elevated temperature. In *Report of the Research Laboratory of Engineering Materials*, number 12, pages 155–172. Tokyo Institute of Technology, 1987.

[65] ACI Committee 318 and American Concrete Institute. *Building Code Requirements for Structural Concrete (ACI 318-11) and Commentary.* American Concrete Institute, 2011.

[66] Z.P. Bažant and P.C. Prat. Effect of temperature and humidity on fracture energy of concrete. *ACI Materials Journal*, 85, 1988.